Neuroleptic malignant syndrome in a 4-year-old girl associated with alimemazine

van Maldegem, Bianca T; Smit, Leo M E; Touw, Daan J; Gemke, Reinoud J B J

Astronomy
&
Astrophysics

Neutral hydrogen and optical observations of edge-on galaxies: Hunting for warps[*]

I. García-Ruiz[1], R. Sancisi[2,1], and K. Kuijken[1]

[1] Kapteyn Astronomical Institute, Postbus 800, 9700 AV, Groningen, The Netherlands
[2] Osservatorio Astronomico di Bologna, Via Ranzani 1, 40127 Bologna, Italy

Abstract. We present 21-cm HI line and optical R-band observations for a sample of 26 edge-on galaxies. The HI observations were obtained with the Westerbork Synthesis Radio Telescope, and are part of the WHISP database (Westerbork HI Survey of Spiral and Irregular Galaxies). We present HI maps, optical images, and radial HI density profiles. We have also derived the rotation curves and studied the warping and lopsidedness of the HI disks. 20 out of the 26 galaxies of our sample are warped, confirming that warping of the HI disks is a very common phenomenon in disk galaxies. Indeed, we find that all galaxies that have an extended HI disk with respect to the optical are warped. The warping usually starts around the edge of the optical disk. The degree of warping varies considerably from galaxy to galaxy. Furthermore, many warps are asymmetric, as they show up in only one side of the disk or exhibit large differences in amplitude in the approaching and receding sides of the galaxy. These asymmetries are more pronounced in rich environments, which may indicate that tidal interactions are a source of warp asymmetry. A rich environment tends to produce larger warps as well. The presence of lopsidedness seems to be related to the presence of nearby companions.

Key words. galaxies: kinematics and dynamics – galaxies: structure

1. Introduction

It has long been known that many galaxies have warped disks. The phenomenon occurs at large galactocentric radii, starting close to the edge of the optical disk. This makes 21-cm line observations essential for the study of warps: there are galaxies that have no optical warp and yet exhibit extraordinary warps in their outer HI layers.

The first indication that the HI distribution of disk galaxies was sometimes bent or warped came in 1957 from observations of our own Galaxy (Burke 1957; Kerr 1957). Early calculations showed that the tidal field due to the Magellanic Clouds was unable to account for the warp of the Galaxy (Burke 1957; Kerr 1957; Hunter & Toomre 1969), and so it was regarded as a rare, uncommon phenomenon. Later on, Sancisi (1976) studied the HI layer of 5 edge-on galaxies and discovered 4 of them to have warps. This result indicated that warps are very common among galaxies. This discovery was not expected, because three of Sancisi's galaxies were quite isolated and thus presented a problem with the tidal-warp scenario. The high incidence of warps among spiral galaxies has later been confirmed with larger

samples both in the optical (Sánchez-Saavedra et al. 1990), (Reshetnikov & Combes 1998) and the HI (Bosma 1991). The ubiquity of warps means that either warps are long-lasting phenomena or they are transient but easily and often excited. Neither of these has been proven and no satisfactory explanation has been found yet. A study by Briggs (1990) of a sample of 12 galaxies showed that: (1) warps start around $R_{25}-R_{H_0}$; (2) the line of nodes of the warp is straight inside R_{25}, and is a leading spiral outside.

The absence of a mechanism that would regularly generate warps and the fact that the line of nodes of the observed warps does not show a severe winding effect (Briggs 1990) suggest that warps are long-lived. The main issue in trying to explain a long lasting warp is differential precession, which in a few rotation periods will destroy the coherent warp pattern (this is similar to the winding problem of material spiral arms). The differential precession arises from the non-sphericity of the potential (Avner & King 1967). However, the survival time of a coherent warp pattern can be larger if the halo in which the disk is embedded deviates only slightly from spherical symmetry (Tubbs & Sanders 1979). Likewise, a halo with a flattening that decreases outwards in the right way would be able to maintain a coherent warped disk for a Hubble time (Petrou 1980).

Extending the work of Hunter & Toomre (1969), Sparke & Casertano (1988) studied long-lived warping modes of a galactic disk inside an oblate halo potential, where no winding

[*] Full Fig. 13 is only available in electronic form at
http://www.edpsciences.org

occurs. They found that the combined torque from a halo and a self-gravitating disk allows a configuration in which the precession frequency of the warp is the same at all radii, thus allowing the warp to maintain its shape unchanged for many rotation periods. One of their assumptions was that of a fixed halo potential that does not react to the potential of the disk.

The back-reaction of the precessing disk onto the halo, analogous to dynamical friction, was investigated by Dubinski & Kuijken (1995), Nelson & Tremaine (1995), and Binney et al. (1998) after an earlier investigation in terms of WKB density waves by Bertin & Mark (1980). It turns out that it has a very strong influence on the evolution of the warp, causing the disk and halo to reorient to a common plane of symmetry in a few orbital times, and making the warp decay.

More recently, several other mechanisms have been investigated. Debattista & Sellwood (1999) studied the warps generated by a disk embedded in a halo whose angular momentum vector is misaligned with that of the disk, and Ing-Guey & Binney (1999) built a model of a warp caused by a disk embedded in a halo which is constantly accreting material of angular momentum misaligned with that of the disk. Magnetic fields have also been proposed as a cause for warps. This hypothesis is mainly based on the alignment of the warps of different galaxies that are close in space (Battaner et al. 1990). Such alignment would be hard to explain in a warping model that is based only on the interaction of a disk and a halo of an individual galaxy without involving the surroundings.

In spite of the several models proposed, none is fully convincing, and many questions remain. Observationally the main problem lies in the fact that the current sample of warped galaxies is very small and inhomogeneous, and often the resolution of the data is poor. Furthermore, in many cases the warps are inferred by modeling the HI kinematics, using assumptions like axisymmetry and circularity of the orbits, which may be not completely correct.

Although most of the warps start outside the optical disk, optical warps do exist. In fact, Sanchez-Saavedra et al. (1990) claimed that the majority of galaxies have optical warps. A study by Reshetnikov & Combes (1998) on optical warps showed the influence of the environment, in the sense that there are more optically warped galaxies in dense environments than in low-density regions. The relation between the optical and HI warps is not clear yet. There have been claims based on near infrared data (DIRBE) that the Galactic warp is more pronounced in the HI than in the old stellar population (Porcel et al. 1997), but an early cutoff of the old stellar disk (Robin et al. 1992) can also explain the data. If magnetic fields have some influence in exciting and/or maintaining warps, the old stellar disk is expected to have a milder warp than the HI disk at every radius (Porcel et al. 1997).

Our goal in this paper is to present an analysis of a sample of late-type spiral galaxies to determine the occurrence rate of warps, and to study their properties (symmetry, dependence on environment, etc.). We have selected a sample of edge-on galaxies that have been observed with the Westerbork Synthesis Radio Telescope (WSRT) for the WHISP project (Swaters et al. 2001). We have used optical R-band data as well (Swaters & Balcells 2002), to explore possible links between the optical properties and the warps of our galaxies. These images also serve to study the environment of our sample galaxies and to identify possible satellite dwarf galaxies that may be orbiting them.

2. The sample

The WHISP sample (Swaters et al. 2001) was selected from the Uppsala General Catalogue of Galaxies (Nilson 1973). Only the galaxies north of 20° declination and with blue diameters larger than 1.5′ were selected. The galaxies are generally larger in HI than in the optical, and with the typical beam size of the WSRT ($12'' \times 12''/\sin\delta$) they are well resolved.

In order to be sure of a sufficiently high signal-to-noise ratio, only galaxies that had a flux density larger than 100 mJy were included in the WHISP sample.

From this sample of 409 galaxies, we selected those that were highly inclined, to be able to observe the warping of the HI layer directly instead of having to infer it from the kinematics. For this purpose, galaxies with optical inclination angles larger than 75° were selected (we assumed an intrinsic axis ratio of 0.2 to calculate the inclination angles). The WHISP database was not yet complete when this project started (August 1999), thus our sample was formed from the galaxies with data available at that time. These are listed in Table 1. A key property of the sample is that it was unbiased towards the existence of warps in the selected galaxies.

Note that nearby large galaxies, which have already been studied in the past have not been re-observed in the WHISP project yet, and are therefore absent from our sample. Including galaxies from the literature might bias the sample towards more "interesting" galaxies.

3. Optical observations and reduction

For most of the galaxies in our sample there are R-band optical data obtained with the Isaac Newton Telescope at La Palma (Swaters & Balcells 2002). These data serve to study the morphology of the galaxies and to search for possible satellites which might have an influence in the bending of the HI disks. The observing procedure and data processing (bias, flat field, calibration) are described in Swaters (1999). There are three galaxies for which data from the INT could not be obtained: for UGC 2459 and UGC 8396 we used data from the Digital Sky Survey, and data for UGC 6964 were kindly provided by Verheijen (1997).

The apparent B magnitudes for the galaxies in the sample have been obtained from the LEDA catalogue (http://leda.univ-lyon1.fr), after correction for inclination and Galactic extinction.

We have used two quantities to measure the extent of the optical disk. The first one is R_{25}, the radius where the R band surface brightness falls to 25 mag/arcsec^2, which we have taken from the LEDA database.

Photometric radii, and especially the not very deep ones like R_{25}, are not always good indicators for the size of a disk. To circumvent this problem, we have estimated the size of the galaxy (R_{opt}) by visually inspecting the images of each galaxy

Table 1. Optical properties of the galaxies in the sample: Galaxy name (UGC and NGC numbers), Hubble type, R_{25}, R_{opt} (see Sect. 3 for definition), inclination angle, position angle of the major axis, apparent b magnitude, corrected for inclination and galactic extinction, error in the magnitude, distance derived with a Virgocentric inflow model, and Tully-Fisher distance. All the data have been extracted from the LEDA database, except for the distances (see Sect. 4.2). We have not used the corrected b magnitude of UGC 2459 because it is not reliable due to its low galactic latitude.

UGC	NGC	type	R_{25} ′	R_{opt} ′	i °	PA °	B_c	ΔB	d_V Mpc	d_{TF} Mpc
1281		Sc	2.23	2.59	90.0	38	10.95	0.11	5.4	5.1
2459		Scd	1.24	2.02	90.0	62	–	–	36.3	36.3
3137		Sbc	1.78	2.66	90.0	74	13.61	1.00	18.3	33.8
3909		SBc	1.32	1.39	90.0	82	13.57	0.77	17.7	24.5
4278		SBc	2.27	2.69	90.0	172	11.09	0.23	10.4	8.1
4806	2770	Sc	1.83	2.41	77.0	148	11.62	0.07	29.6	21.0
5452	3118	Sc	1.26	1.41	90.0	41	12.88	1.00	22.1	21.7
5459		SBc	2.38	2.67	90.0	132	11.58	0.11	19.6	15.9
5986	3432	SBd	3.44	3.52	81.2	38	10.36	0.08	8.9	8.5
6126	3510	SBcd	2.03	2.13	90.0	163	11.17	0.33	8.8	8.8
6283	3600	Sab	2.03	2.15	87.0	3	11.51	0.59	11.4	11.3
6964	4010	SBcd	2.10	2.13	85.5	66	11.79	0.10	16.6	16.9
7089		Sc	1.61	2.73	87.2	36	12.29	0.14	13.2	11.6
7090	4096	SBc	3.30	3.96	80.9	20	10.16	0.19	9.4	10.2
7125		SBd	2.35	2.26	90.0	85	12.44	0.92	19.6	12.6
7151	4144	SBc	3.06	3.34	81.6	104	10.72	0.16	4.3	6.0
7321		Sc	2.78	2.91	90.0	82	11.99	0.16	4.0	14.9
7483	4359	SBc	1.75	2.49	80.8	108	12.31	0.80	22.4	17.6
7774		Sc	1.75	1.90	90.0	102	12.98	0.86	7.3	20.6
8246		SBc	1.71	1.86	90.0	83	13.62	1.00	11.7	19.4
8286	5023	Sc	3.03	3.58	90.0	28	11.09	0.13	6.3	8.0
8396	5107	SBc	0.84	0.90	77.3	128	13.89	1.45	17.4	27.5
8550	5229	SBc	1.67	2.10	90.0	167	12.97	1.00	6.3	13.2
8709	5297	SBbc	2.72	3.02	83.6	148	11.13	0.21	37.3	19.8
8711	5301	SBc	2.02	2.49	87.2	151	11.98	0.22	25.8	22.5
9242		Sc	2.51	3.04	90.0	71	11.86	0.07	24.7	12.6

in the sample and determining where the disk ends. These radii are listed in Table 1. They are larger than R_{25}, in some cases by more than 50%. They are somewhat subjective but do provide a useful lower limit to the optical size of the galaxy.

4. HI observations and analysis

The HI observations were obtained with the WSRT between 1995 and 1998. Most galaxies were observed for 12 hours. The typical beam size is $12'' \times 12''/\sin\delta$, the channel separation 4.14 km s^{-1} for most of the galaxies, and 16.7 km s^{-1} for the most distant ones. The observational parameters, exposure time, resulting beam size and other relevant data are given in Table 2. The primary beam is about 37′.

The reduction was done using the WHISP reduction pipeline. The detailed information about the reduction steps can be found in the WHISP web pages, `http://www.astro.rug.nl/~whisp`. This results in 3 sets of channel maps for each galaxy: at full resolution, at 30′′ and at 60′′.

The HI data presented in this article in Fig. 7 (rotation curves, HI radial surface density profiles and warp curves) and in Fig. 13 (6 panel figures for each galaxy) is also available in electronic form in the WHISP pages

(`http://www.astro.rug.nl/~whisp`), together with some other diagrams that supply extra velocity information.

4.1. Global HI line profiles, HI masses and total HI maps

The global HI line profiles were determined by adding the intensities of the CLEAN components from the 60′′ Hanning smoothed datacube, corrected for primary beam attenuation.

The total HI masses were derived according to the formula

$$M_{HI} = 2.36 \times 10^5 D^2 \int S \, dV \tag{1}$$

where M_{HI} is the total mass in $M_\odot$, D is the distance to the galaxy in Mpc, S is the flux density in Jy and the integral is made over all the velocities in km s^{-1}.

To construct the total (integrated over velocity) HI maps, we used the same masks already used in the CLEANing to define the areas of emission. Outside these areas the maps were set to zero to avoid adding unnecessary noise to the total HI map. Then all the masked channels were added, creating the column density map.

This is a standard procedure which allows a higher S/N ratio to be obtained, but it has the disadvantage that the noise level is not the same everywhere across the map. This is

Table 2. Observation parameters for the HI synthesis data: Galaxy UGC number (1), Length of the observation in hours (2), Date of observation (3), RA (4) and Dec (5) of the field center, central observing frequency (6), corresponding heliocentric velocity (7), synthesized beam in both RA and Dec directions (8), total bandwidth (9), number of channels (10), velocity resolution (11), rms noise of the resulting datacube (12), conversion factor from flux density to brightness temperature (13).

Galaxy UGC	T_{obs} hours	Date	RA (1950)	Dec (1950)	f_{cen} MHz	V_{hel} km s^{-1}	S. beam $\alpha \times \delta$ ''	Bw MHz	N_{ch}	res_{vel} km s^{-1}	rms mJy/beam	T_B/S K/mJy
(1)	(2)	(3)	(4)	(5)	(6)	(7)	(8)	(9)	(10)	(11)	(12)	(13)
1281	12	08 Nov. 95	01 46 39	32 20 39	1419.79	157	11.14 × 20.96	2.48	127	5.0	3.2	2.6
2459	12	04 Jun. 97	02 57 06	48 49 59	1408.75	2464	13.08 × 17.17	4.92	63	20.1	2.1	2.7
3137	12	24 Jan. 96	04 39 24	76 19 59	1415.64	1020	11.70 × 11.88	2.48	127	5.0	2.9	4.4
3909	12	11 Jun. 97	07 30 52	73 49 27	1415.86	945	11.38 × 11.83	2.48	127	5.0	3.3	4.5
4278	12	01 Apr. 96	08 10 27	45 53 49	1417.68	581	12.05 × 17.23	2.48	127	5.0	2.8	2.9
4806	12	16 Jun. 97	09 06 29	33 19 37	1411.09	1951	12.57 × 23.85	4.92	63	20.0	1.8	2.0
5452	24	23 Jun. 97	10 04 17	33 16 27	1413.95	1342	12.06 × 22.43	2.48	127	5.0	2.5	2.3
5459	12	24 Nov. 97	10 04 54	53 19 36	1415.15	1111	14.39 × 17.89	2.48	127	5.0	4.1	2.4
5986	12	09 Feb. 96	10 49 42	36 53 04	1417.46	616	11.34 × 19.29	2.48	127	5.0	3.3	2.8
6126	36	17 Nov. 97	11 01 01	29 09 19	1416.99	705	12.47 × 27.34	2.48	127	5.0	2.6	1.8
6283	12	19 Sep. 97	11 13 06	41 51 48	1416.90	719	12.50 × 18.73	2.48	127	5.0	3.0	2.6
6964	12	12 Mar. 98	11 56 03	47 32 20	1416.11	907	10.24 × 13.29	2.48	127	5.0	1.8	4.5
7089	12	27 Oct. 97	12 03 26	43 25 37	1416.67	776	12.87 × 18.76	2.48	127	5.0	3.3	2.5
7090	12	03 Nov. 97	12 03 28	47 45 12	1417.64	566	12.48 × 17.15	4.92	63	19.9	1.7	2.8
7125	12	29 Nov. 96	12 06 10	37 04 51	1415.32	1071	12.32 × 20.54	2.48	127	5.0	3.3	2.4
7151	12	02 May 97	12 07 28	46 44 07	1419.13	267	12.24 × 17.03	2.48	127	5.0	3.2	2.9
7321	13	10 Nov. 97	12 15 02	22 49 00	1418.39	409	12.14 × 32.76	2.48	127	5.0	3.5	1.5
7483	12	12 Nov. 97	12 21 42	31 47 57	1414.39	1253	11.88 × 24.21	2.48	127	5.0	3.4	2.1
7774	24	10 Dec. 97	12 33 57	40 16 49	1417.83	526	10.67 × 16.93	2.48	127	5.0	2.4	3.4
8246	12	22 Dec. 97	13 07 44	34 26 48	1416.49	813	12.05 × 22.71	2.48	127	5.0	3.1	2.2
8286	24	20 Dec. 96	13 09 58	44 18 13	1418.40	407	12.30 × 18.11	2.48	127	5.0	2.3	2.7
8396	12	05 Jan. 98	13 19 09	38 47 58	1415.86	946	12.15 × 20.27	2.48	127	5.0	3.5	2.5
8550	11	12 Dec. 96	13 31 58	48 10 16	1418.61	364	12.88 × 16.75	2.48	127	5.0	3.6	2.8
8709	12	09 Jan. 98	13 44 19	44 07 23	1409.03	2407	12.56 × 18.56	4.92	63	20.1	1.7	2.6
8711	12	12 Jan. 98	13 44 21	46 21 28	1413.26	1503	10.87 × 15.04	4.92	63	20.0	1.7	3.7
9242	12	26 Nov. 98	14 23 59	39 45 00	1413.40	1470	9.83 × 15.28	2.48	127	5.0	3.1	4.1

caused by the fact that at each position of the map a different number of channels are added. We can calculate the noise at each position as

$$\sigma_{tot} = n_l^{0.5} \sigma_{cs} \sqrt{(n_c + n_l)/(n_c - 1)} \qquad (2)$$

where σ_{tot} is the noise in the total HI map and σ_{cs} is the noise in the fit to the line-free channels used to form the continuum. The number of channels contributing to the total HI map is given by n_l and the number of continuum channels by n_c (see Verheijen & Sancisi 2001 for the derivation of this formula). This expression is used to calculate the noise at each position in the total HI map, and to construct the map with the S/N ratios. We then calculated the average noise value of all the points in this map which had $2.75 < (\frac{S}{N}) < 3.25$, and adopted this as the "3σ" contour level. This threshold is indicated by a thick line in the total HI maps of the Atlas (see Fig. 13).

Finally, we corrected the map for primary beam attenuation.

The global HI profiles, total HI maps, and position-velocity (XV) diagrams along the major axis of each galaxy are shown in Fig. 13.

4.2. Distance determination

In order to determine the distance to each galaxy in the sample we first tried a simple Virgocentric inflow correction, as described in Kraan-Korteweg (1986) with a Hubble constant of $H_0 = 75$ km s^{-1} Mpc^{-1}.

Figure 1 shows the Tully-Fisher (TF) relation for our sample obtained using the derived distances. We took the corrected apparent magnitudes from the LEDA catalogue, and determined the absolute magnitudes with the "virgocentric" distances. The widths of the profiles were corrected for instrumental broadening (following Bottinelli et al. 1990) as well as for inclination. The dotted line in Fig. 1 is the TF relation derived by Verheijen (1997) for the B band. Some points do clearly follow the relation, but there are many outliers. Some of the deviations are greater than 1.5 mag (a factor of two in distance). There are various indications that the Virgocentric inflow model may not give the correct distances: the first is that when one looks at the distribution of galaxies in supergalactic coordinates, the galaxies with large discrepancies are not randomly distributed on the sky, but grouped together. Another indication that there could be problems with such simple, spherical virgocentric inflow model is the fact that the Virgo Cluster may be far from spherical (West & Blakeslee 1997). This will
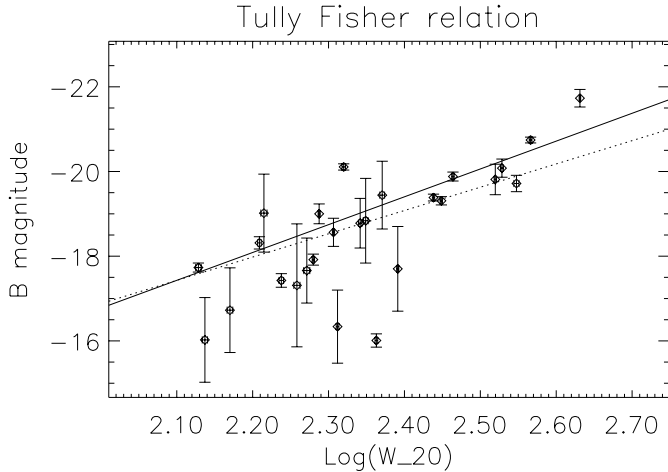
Fig. 1. *B* band Tully-Fisher relation for the galaxies in the sample. We have taken apparent *B* magnitudes from the LEDA database, and converted them to absolute magnitudes with the distance determined as explained in Sect. 4.2. The dotted line is the TF from Verheijen (1997), the solid line indicates the fit to the data.

probably affect quite strongly the distance determination for nearby galaxies.

We have, therefore, decided to calculate the distances using the TF relation. The estimated distance uncertainty introduced by this is expected to be 30% (0.6 mag). Of course, galaxies for which the apparent magnitude already has a large error will have a more uncertain distance.

4.3. Determination of the center of the galaxies

It is necessary to know the position of the center of a galaxy to be able to determine its rotation curve, its lopsidedness and the warp asymmetry. In an axisymmetric galaxy with gas in circular orbits this location is at the same time the center of the potential, the center of the gas orbits, and the point of maximum optical emission (if dust absorption is not very important). In the case of an asymmetric galaxy, the center can be determined in several ways:

If the galaxy has a nuclear radio continuum source, this marks the position of the center with great accuracy. But this is rare.

The center may also be derived from ellipse fitting to the optical isophotes. This method has the problem that it is very sensitive to dust, and can lead to large errors. Similarly, ellipses can be fitted to the total HI maps, but since the HI often has a lot of substructure such fits are unreliable.

In both HI and optical ellipse fitting, one gets a set of ellipses (thus, a set of centers) and has to extract a single center from it. Sometimes this is easy and the weighted mean of all those centers is a good measure of the "true" center, but when the galaxy is lopsided this is no longer the case and a linear fit to the centers derived from the fits is necessary to find the center of the galaxy.

Another method is based on the position-velocity (XV) diagram along the major axis of the galaxy and consists in finding the center that minimizes the asymmetries of the XV diagram.

In this way one can be sure that the derived asymmetries are a lower limit to the true asymmetries of the galaxy. Density and kinematic information are thus combined in this method, which uses the whole XV diagram and not only the rotation curve or only the density profile. The center is determined in the following way:

1. Symmetrization of the XV diagram: the XV diagram is mirrored with respect to an initially adopted center, and added to the original XV diagram. In this way we create a symmetric image that will resemble the original one if the center is correct and the galaxy is symmetric;
2. We cross-correlate the symmetrized XV with the original XV and find where the peak of the resulting image lies. This gives us the distance and direction we need to move our center from the previously adopted one;
3. Steps (i) and (ii) are repeated until convergence is achieved. The method has proved to be very robust and converges in very few iterations.

The centers used in this article were derived using a mixed approach: first, the center was determined using the ellipse-fitting method to the optical images. To determine the position angle we used both the HI and optical ellipse fits. If the optical position angles gave a consistent result, we chose that one. If, instead, the ellipses were strongly influenced by dust or bright star wings, then we chose the position angle determined from the HI ellipse fits.

With a position angle and a center, we extracted the XV diagram along the major axis defined by these quantities. At this point we applied the "XV-method" to improve the determination of the position of the center. Table 3 lists the positions of the centers obtained with this method as well as those listed in LEDA. The distances between both centers are usually not larger than 4″ and there is only one case exceeding 10″ found for UGC 5986, a very distorted galaxy both kinematically and morphologically.

4.4. HI profile and radius

In highly inclined systems, each line of sight to the galaxy contains information about different portions of that galaxy. At each position (see Fig. 2) we get the integrated signal coming from different radii, and we have to disentangle that information to get the radial density profile.

This has been done following the procedure developed by Warmels (1988). First, all the emission from the galaxy is integrated in the direction perpendicular to the major axis, resulting in an HI strip integral. This is then deconvolved using the Lucy (1974) deconvolution scheme, assuming that the HI distribution is axisymmetric, and taking into account the size of the beam. This algorithm has been applied separately to the two sides of the galaxy. This allows us to estimate the density lopsidedness in the HI gas by comparing one side with the other.

The HI radius (R_{HI}) has been calculated using the average of the two deconvolved profiles, and is defined as the radius where the HI surface density drops to $1\ M_{\odot}/pc^2$.

Table 3. Comparison between the positions of the centers listed in LEDA (Cols. 2, 3) and the ones adopted in this work (Cols. 4, 5). The distance between the two centers is listed in Col. 6.

| UGC	RA$_{2000}$ LEDA	Dec$_{2000}$ LEDA	RA$_{2000}$ XV	Dec$_{2000}$ XV	dist ($''$)
1281	01 49 32.0	32 35 21.5	01 49 31.7	32 35 16.2	6.2
2459	03 00 37.1	49 02 41.3	03 00 36.5	49 02 34.2	9.0
3137	04 46 16.0	76 25 07.2	04 46 15.5	76 25 06.4	2.1
3909	07 36 59.1	73 42 50.1	07 36 58.8	73 42 48.9	1.7
4278	08 13 58.8	45 44 35.2	08 13 59.0	45 44 38.0	3.7
4806	09 09 33.5	33 07 29.4	09 09 33.8	33 07 25.1	5.8
5452	10 07 11.5	33 01 38.4	10 07 11.6	33 01 39.3	2.0
5459	10 08 10.1	53 04 58.4	10 08 10.3	53 04 58.9	2.2
5986	10 52 30.9	36 37 03.4	10 52 31.7	36 37 16.3	17.
6126	11 03 43.6	28 53 05.6	11 03 43.6	28 53 07.3	1.7
6283	11 15 52.1	41 35 32.2	11 15 52.1	41 35 27.6	4.7
6964	11 58 37.1	47 15 37.1	11 58 37.1	47 15 35.1	2.1
7089	12 05 57.7	43 08 35.3	12 05 58.0	43 08 37.2	3.6
7090	12 06 01.5	47 28 47.6	12 06 01.2	47 28 40.4	7.9
7125	12 08 42.2	36 48 07.8	12 08 42.3	36 48 08.5	1.1
7151	12 09 58.7	46 27 26.5	12 09 58.1	46 27 27.8	6.6
7321	12 17 33.9	22 32 25.0	12 17 34.0	22 32 25.1	1.5
7483	12 24 11.4	31 31 17.5	12 24 11.8	31 31 14.9	5.1
7774	12 36 23.1	40 00 17.8	12 36 23.0	40 00 18.4	0.8
8246	13 10 04.2	34 10 52.5	13 10 04.4	34 10 49.8	3.3
8286	13 12 11.8	44 02 14.8	13 12 11.7	44 02 13.2	1.8
8396	13 21 24.7	38 32 15.7	13 21 24.9	38 32 16.9	2.6
8550	13 34 03.1	47 54 45.2	13 34 03.0	47 54 47.3	2.6
8709	13 46 23.8	43 52 20.3	13 46 23.8	43 52 18.9	1.4
8711	13 46 24.7	46 06 28.2	13 46 24.6	46 06 24.6	3.8
9242	14 25 20.8	39 32 21.1	14 25 20.6	39 32 19.4	2.8
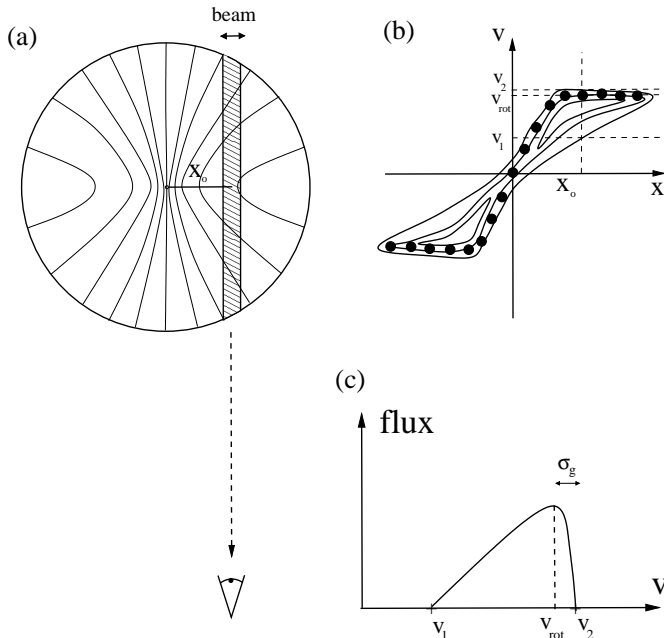
Fig. 2. Schematic representation of the HI detected at each position along the major axis in an edge-on galaxy. **a)** At a certain distance x_0 from the center of the galaxy, all the emission from gas in the dashed area is detected by the telescope. Isovelocity lines (with respect to the observer) have been drawn in the figure. The XV diagram along the major axis with the rotation curve (filled dots) is shown in **b)**, and a velocity profile at a certain major axis distance (x_0) in **c)**. The rotation velocity at x_0 is indicated by v_{rot}, where σ_g is the broadening due to instrumental and random motion effects.

4.5. Rotation curves

The determination of a rotation curve for a highly inclined galaxy is not simple. The most satisfactory approach would be to model the kinematics of the galaxy as a whole (Swaters 1999), but in an edge-on galaxy there are many parameters to be fitted: the radial HI profile, the warp profile and its line of nodes, and the rotation curve. Furthermore we are also trying to determine deviations from axisymmetry.

For these reasons, we have focused on the derivation of the rotation curve from the position-velocity (XV) diagram along the major axis of the galaxy. In galaxies with low inclinations, the beam samples the HI emission from a small portion of the disk, and the profiles in the XV diagram are basically Gaussian, unless beam-smearing plays an important role. In a completely edge-on galaxy, however, the beam intercepts a large portion of the disk, as illustrated in Fig. 2. In this case, the derivation of the rotation curve can be done as outlined in Sancisi & Allen (1979). At each position along the major axis the maximum rotation velocity (relative to the systemic) is chosen, corrected for the instrumental broadening and random motions of the gas. This method assumes that there is gas everywhere along the line of sight, and may give the wrong rotation velocity if this is not the case.

We have determined the velocity at each position along the major axis by fitting half a Gaussian to the edge of the profile at that position. The width of the Gaussian is held fixed with a value of $\sigma_g = \sqrt{\sigma_{instr}^2 + \sigma_{rnd}^2}$, where σ_{instr} is the instrumental
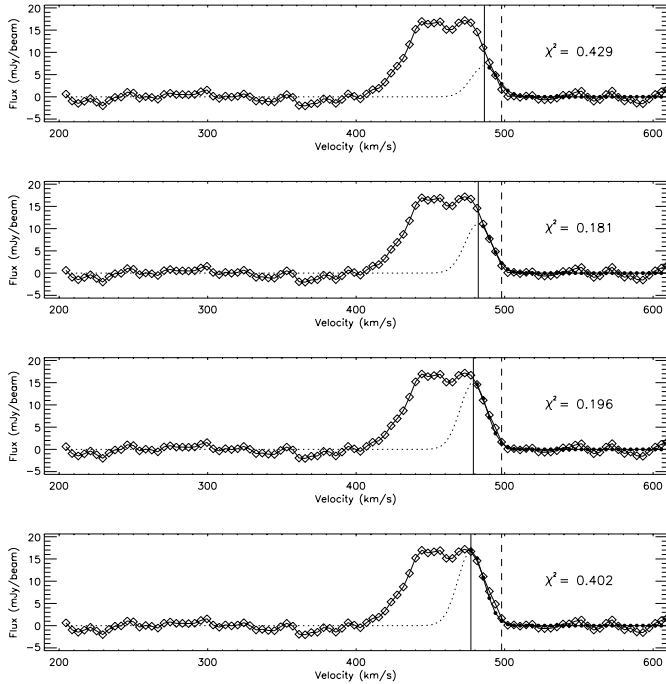
Fig. 3. Edge-fitting method. A profile of UGC 8286 is plotted, along with 4 different fits. The data are displayed as diamonds, and the fit as filled circles and dotted line. The dotted line shows the part of the Gaussian that is not used in the fit. From top to bottom, the fits make use of 2, 3, 4 and 5 "signal" points (points left of the vertical dashed line). Each panel also shows the reduced χ^2 for each fit, and the resulting velocity (solid vertical line). The final parameters are taken from the best fit (in this case, the second panel from the top).

broadening and σ_{rnd} is the velocity dispersion of the gas due to the random motions in the disk. Measurements of velocity dispersion of galaxies in HI give typical values that range from ~10–12 km s^{-1} in the inner parts to ~6 km s^{-1} in the outer parts (Kamphuis 1993; Dickey et al. 1990). Here we have adopted a constant value of 8 km s^{-1} through the whole HI disk, which seems a reasonable assumption.

Figure 3 illustrates how the rotational velocity at each radius is determined. We extract a velocity profile (see Fig. 2) at a position along the major axis, and determine where the emission from the galaxy begins in velocity. This is done by looking where in the profile n_p points lie above 3σ. After some experimentation we have adopted $n_p = 3$. At this moment we make a series of Gaussian fits to the edge of the profile, varying the amount of signal points included in the fit (see Fig. 3). The rotation velocity will be the center of the Gaussian with a smaller reduced χ^2 of all the fits.

The error in the determined rotation velocity is calculated from the amplitude of the fitted Gaussian. This error also depends on the velocity resolution compared to the dispersion of the Gaussian, and on the dispersion of the Gaussian itself. After extensive Monte-Carlo simulations we derived the following formula to calculate the errors for our edge-fitting method:

$$\sigma_v = \frac{4.0\sigma_g}{\sqrt{n_{ps}(\frac{S}{N})}} \tag{3}$$

where σ_v is the error in the rotation curve velocity, σ_g is the dispersion of the Gaussian, n_{ps} is the number of points every σ_g (sampling factor), and S/N is the ratio of the amplitude of the Gaussian to the noise level. This formula is valid for $n_{ps} \gtrsim 2$, and the error increases less than 60% for $n_{ps} \simeq 1$. The typical velocity resolution of our observations has a $FWHM$ of 4 km s^{-1}, so $n_{ps} \simeq 2$.

A rotation curve derived by making edge-fits in the velocity direction as described above still suffers from the effects of beam smearing. The influence of this is to overestimate the velocities in the inner rising parts of the rotation curve and in some galaxies the effect is quite severe. To correct for this we have performed edge-fits in the horizontal direction as well. In these fits the width of the Gaussian depends on the slope of the rotation curve, velocity resolution and the beam width. We determined this width by fitting a full Gaussian around the center of the galaxy.

At this stage we have two determinations of the rotation curve, one from the edge-fits in the velocity direction and the other from those in the spatial direction. The final rotation curve is the minimum of the two determinations.

To assess that the errors are realistic in the rotation curve for each radius and correct artificial "bumps" created by noise in the edge-fits, we determined the mean velocity of the data within a beam size and its dispersion. The mean value is the finally adopted rotation velocity and the error is the sum in quadrature of the formal error and the dispersion.

The rotation velocities were derived separately for the approaching and receding sides, to be able to compare them and to look for kinematic asymmetries.

We would also like to note that a number of galaxies (UGC 5986, 8246, 9242, see XV diagrams in Fig. 13) have non-circular motions in the central regions. This suggests either that orbits in these systems are elliptical, or that there are radial motions of the gas, and caution against the use of our rotation curves as tracers of the inner potential wells of these galaxies.

4.6. Warping

We have derived the curve of the warp from the total intensity maps, by fitting Gaussians to the density profiles parallel to the minor axis of the galaxy. We thereby determine the position of the HI ridge at each radius. This underestimates warps that have a line of nodes significantly different from our line of sight. For example, the ridge of the HI could warp very little, but there may be a low level envelope that bends with greater amplitude, but that would not show up in a Gaussian fit. Thus, the numbers we get from this procedure will have to be treated as lower limits for the warp amplitude.

To characterize this curve by a number, we have, first of all, determined the warp starting radius (r_{warp}). This is the radius where the warp curve leaves significantly the plane defined by the inner parts of the disk. Many factors (as small corrugations and noise in the warp curve) can hamper the determination of the warp radius. To overcome these we have devised a complex procedure which smoothes the data at different
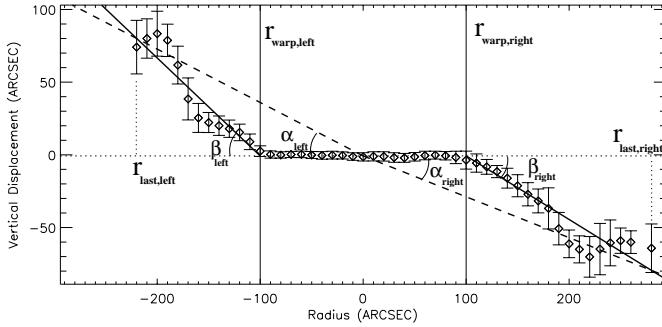
Fig. 4. Determination of the warp angles α_i, for i = left, right. $r_{\text{warp},i}$ is where the warp begins, $r_{\text{last},i}$ the projected distance along the major axis to the last measured point, and β_i the angle between the major axis and the straight line resulting from the fit to the points between those radii.

resolutions and takes the scatter in the inner disk into account (see Appendix A for full details). The warp radius for one side of a galaxy (UGC 6126) was strongly affected by the presence of spiral arms. We manually set the warp radius of that side to that of the other side of the galaxy. Once the warp radius has been determined, a straight line is fitted to the points with $r > r_{\text{warp}}$. With this we calculate the warp angle according to the following definition (see Fig. 4):

$$\tan(\alpha) = \tan(\beta)(r_{\text{last}} - r_{\text{warp}})/r_{\text{last}} \tag{4}$$

where β is the angle resulting from the mentioned fit and r_{last} is the maximum radius at which we can measure the centroid of the HI ridge. Wiggles in the warp curve (caused by not completely edge-on spiral arms, or by warps that bend first to one side and then to the other) can cause important differences in the measured r_{warp}, but we have found that our measure of the warping angle (α) is quite robust to them.

Even though for most galaxies the warps are well represented by this angle, there are some that are not well fitted by a straight line from r_{warp} to r_{last}, either because they rise faster or because the gas layer bends back towards the plane defined by the inner disk, as is the case of the Galaxy (Burton 1988).

The warping angle is calculated separately for both sides of the galaxy, and in this way we can estimate the asymmetry of the warp using the difference between one side and the other. Most of the warps (all except 2 systems that are strongly interacting) have S-shape, i.e. the gas layer bends in opposite directions on either side of the galaxy. Taking into account that the warp angles are measured anticlockwise and that a symmetric S-shape warp would have $\alpha_{\text{left}} = -\alpha_{\text{right}}$ we have defined the warp asymmetry as:

$$\alpha_{\text{asym}} = |\alpha_{\text{right}} + \alpha_{\text{left}}|. \tag{5}$$

4.7. Lopsidedness

There is ample evidence that a large fraction of galaxies depart from axisymmetry. This can be inferred from the asymmetric shape of the global HI profile. Such asymmetry can be caused by either a density asymmetry or a kinematic one. Richter & Sancisi (1994) estimated that at least 50% of the galaxies have

asymmetric global profiles. Later work by Haynes et al. (1998) confirmed this result. Swaters et al. (1999) discussed the lopsidedness in the kinematics and concluded that probably at least half of all galaxies are kinematically lopsided.

We therefore want to find out how lopsided our galaxies are and whether there is any relationship between lopsidedness and warping. This will be investigated both in the kinematics (using the rotation curves from the approaching and receding sides) and in the density.

To quantify the lopsidedness in the HI distribution we have calculated the HI mass for each side of the galaxy (M_1, M_2) and defined the lopsidedness index as

$$\text{Lop}_\rho = \frac{|M_1 - M_2|}{M_1 + M_2}. \tag{6}$$

The kinematic lopsidedness has been derived from the difference in the rotation curves between the receding and the approaching sides (V_r and V_a respectively, defined to be positive). The kinematic lopsidedness index was calculated according to the formula

$$\text{Lop}_{\text{kin}} = \frac{\sum_x V_{\text{dif}}(x)/\sigma_{\text{dif}}^2(x)}{\sum_x 1/\sigma_{\text{dif}}^2(x)}, \tag{7}$$

where

$$V_{\text{dif}}(x) = \frac{|V_a(x) - V_r(x)|}{(V_a(x) + V_r(x))/2} \tag{8}$$

and σ_{dif} are the uncertainties in V_{dif}.

4.8. Environment

One of the issues that we want to address is the role of the environment in warp phenomena. Reshetnikov & Combes (1998) found that the percentage of optically warped galaxies is higher in rich environments. We want to find out if this also holds for the HI warps or not. For that purpose, for each galaxy we have searched in the NASA/IPAC Extragalactic Database (NED) looking for companions which are within 100 arcmin and have a radial velocity difference less than 150 km s^{-1} with respect to our galaxies. We have also looked for companions in our HI datacubes, at full resolution, 30″ resolution, and 60″ resolution. The primary beam at Westerbork has a *FWHM* of about 37′ at 21 cm, which determines how far away from the galaxy we are able to detect other objects. We have listed the companions from NED and those detected in HI in Table 7. We have found two new systems (companions to UGC 4806), and determined velocities for 4 systems that had no previous velocity determination.

With all this information, we have assigned a number to each galaxy depending on how close the companions are: 2 (companion within 50 arcmin), 1 (companion at distance between 50 and 100 arcmin), or 0 (no companions in 100 arcmin).

5. Results

Here we present (Table 4) the determined warp angles, the density and kinematical lopsidedness and the classification according to the environment. We also present the rotation curves, the

Table 4. Results from the HI analysis: Galaxy UGC number (1), kinematical lopsidedness (2), density lopsidedness (3), HI radius (at 1 $M_\odot$/pc^2) (4), total HI mass (5), systemic velocity (6), width of the global profile at 20% (7) and 50% (8) levels, position angle of the major axis (9), warp angles on the East (10) and West (11) sides of the galaxy, environmental classification (12, for definitions see Sect. 4.8).

UGC	Lop$_{kin}$ %	Lop$_\rho$ %	R_{HI} ′	M_{HI} $10^8\,M_\odot$	V_{sys} km s^{-1}	W_{20} km s^{-1}	W_{50} km s^{-1}	PA °	Warp$_1$ degree		Warp$_2$ degree		Env
(1)	(2)	(3)	(4)	(5)	(6)	(7)	(8)	(9)	(10)		(11)		(12)
1281	3.1	0.0	3.40	1.2	157	132.4	123.3	39	5.3 ±	0.7	−0.7 ±	0.7	0
2459	2.2	7.4	3.87	134.1	2465	335.5	324.7	64	−4.4 ±	0.6	1.4 ±	1.1	2
3137	6.0	4.0	3.53	32.2	992	243.3	232.2	74	−2.7 ±	0.5	3.3 ±	0.7	0
3909	1.7	0.4	2.29	10.4	943	183.6	167.6	80	−4.9 ±	2.6	8.8 ±	1.7	0
4278	7.2	1.8	3.13	10.2	558	192.8	173.5	173	−		−2.9 ±	0.6	2
4806	1.2	0.3	2.33	72.1	1950	351.6	328.1	148	3.2 ±	1.4	−		2
5452	3.1	9.3	1.94	23.3	1340	220.8	203.0	38	−4.7 ±	2.1	17.4 ±	2.3	2
5459	9.2	3.0	3.58	37.3	1108	287.6	269.0	131	−8.1 ±	3.1	3.1 ±	0.9	1
5986	5.4	6.9	5.29	27.1	624	265.6	243.1	38	4.6 ±	0.7	22.4 ±	3.0	2
6126	3.7	11.6	3.07	10.3	701	198.7	184.8	166	−18.6 ±	1.1	26.5 ±	1.1	2
6283	2.9	0.4	3.48	15.1	715	214.9	201.8	8	6.1 ±	1.8	−3.5 ±	1.3	0
6964	5.4	3.2	2.83	19.0	906	274.4	262.7	65	20.2 ±	1.3	−15.7 ±	0.8	1
7089	13.4	15.1	2.13	5.8	782	158.3	141.7	36	−		−		2
7090	9.8	10.2	3.82	12.9	575	341.3	312.8	20	−		−		2
7125	5.6	9.5	3.70	34.2	1079	161.9	147.6	83	−		5.9 ±	0.6	2
7151	8.6	0.4	3.26	1.9	265	167.6	157.0	102	−		−		1
7321	2.4	1.5	3.23	2.4	407	230.2	220.9	82	−		−2.6 ±	0.8	0
7483	2.5	2.7	2.47	21.1	1247	227.1	198.8	108	−		−		2
7774	5.2	1.9	2.72	3.4	522	203.3	190.3	102	15.2 ±	2.5	−32.8 ±	2.7	1
8246	3.9	1.8	2.19	4.8	809	145.4	134.6	83	−		−17.0 ±	2.5	2
8286	2.1	0.6	4.25	5.4	406	188.9	179.0	28	−2.3 ±	0.5	4.6 ±	1.0	0
8396	7.4	4.9	1.78	9.8	951	173.3	142.2	128	−		23.9 ±	6.7	2
8550	1.9	3.6	2.85	2.0	359	135.4	124.4	167	2.5 ±	1.0	−		1
8709	4.4	9.5	3.46	174.2	2410	416.5	399.1	148	−		−		2
8711	3.9	0.7	3.10	53.8	1506	330.5	311.2	151	−16.4 ±	2.7	8.7 ±	1.7	0
9242	6.8	2.9	3.13	31.0	1439	208.5	195.1	72	−		−		1

Table 5. Different types of warps depending on the environment. Each column represents a different environment (for details see Sect. 4.8). The first row is for galaxies with no warp, the second for galaxies with a warp on only one side, and the third is for galaxies that show a warp on both sides of their disks. The last row lists the total number of warped galaxies for each environment. Numbers in brackets count a side of a galaxy as warped only if it warps more than 2° within the errors.

	Total	Poor	Intermediate	Rich
Total	26	7	6	13
No warp	6 (9)	0 (1)	2 (3)	4 (5)
1-warps	7 (7)	1 (2)	1 (0)	5 (5)
2-warps	13 (10)	6 (4)	3 (3)	4 (3)
All warps	20 (17)	7 (6)	4 (3)	9 (8)

radial density profiles, and the warp curves in the combined plots of Fig. 7.

Finally, we study the influence of the environment on warping and lopsidedness, and we compare the optical and HI warps of a number of galaxies.

5.1. Warp statistics and shapes

The first question to address is how common warps are. Table 4 already shows that the outer parts of the majority of galaxies exhibit some departure from flat disks. We detect warps in 20 of our galaxies, of which 7 show a warp only on one side (see Table 5). If we consider only warps larger than 2°, the number of warps decreases to 17, of which 7 are only on one side. Taking into account that we will probably miss most of the warps with a line of nodes close to the direction perpendicular to the line of sight from us to the galaxy, it means that the vast majority of galactic disks are warped.

Warps normally start at the edge of the optical disk or further away. This means that for the warp to be visible there must be gas outside the optical disk. We looked at the galaxies in our sample with no warp to see if any of them had extended HI disks, i.e. if there was any galaxy with an extended HI disk (with respect to the optical emission) and no warp. As a measure of the optical extent of the galaxy we used R_{opt} (see Sect. 3), which is more representative than R_{25}, particularly in edge-on galaxies. We found that all the galaxies in our sample that have HI disks more extended than the optical are warped. If we consider each side of the galaxy independently, there is only one exception to this rule: one side of UGC 7125 is warped, while the other remains flat, and both sides have HI more extended than the optical.

One of the most striking characteristics of the warps observed here is their asymmetry. To begin with, a considerable percentage of the warped galaxies show a warp only on one

side. This is not due to an absence of HI on the opposite side: in all cases the gas disk on the unwarped side does extend to beyond R_{warp}. Sometimes (as in UGC 7321, 8246, 8396) there are hints of the beginning of a warp in that side but the data do not allow a firm detection of it.

However, the clearest sign of asymmetry in warps comes from galaxies with both sides warped. Figure 5 shows the warp asymmetry (α_{asym}) with respect to the mean warp angle. Only galaxies with warps detected on both sides of the disk are plotted. We inspected the total HI maps of all our galaxies looking for tidal features that would clearly indicate strong tidal interaction with a nearby companion. Such interaction might produce a highly asymmetric warp. These galaxies are plotted as filled circles in Fig. 5, and indeed they appear to possess more asymmetric warps than the rest of the galaxies. But the remaining warped galaxies also have large asymmetries. There are only 2 systems with large warps and high symmetry: UGC 6964 and UGC 6126. The other galaxies lie more or less on a straight line where the ratio of the asymmetry to the mean warp is of about 0.7. A galaxy with this asymmetry and a mean warp of 10° would have warps in each side of 6.5° and 13.5°, which is quite asymmetric.

Most of the galaxies with both sides warped are antisymmetric (S shape warps). We only have two cases of U-type warps, and both these galaxies are strongly interacting with nearby companions and are very disturbed.

The warp curves, together with the rotation curves and the radial density profiles have been plotted in Fig. 7. These plots show the shapes and amplitudes of the warps, and allow a comparison between features in the radial density profiles, rotation curves and warp curves. It is quite clear from Fig. 7 that there are several distinct warp shapes: some galaxies have monotonically increasing warps (rising linearly or even faster), while others have warps that at some point rise slowly, and in some cases head back to the plane defined by the inner regions, like the southern warp in the Milky Way. Note that the rotation curves in Fig. 7 have been calculated along the major axis and not along the warp line. This is the reason why the rotation curves often stop before the HI density drops to zero, as in UGC 6964.

5.2. Lopsidedness

Lopsidedness may have some connection with warping. If, for instance, the lopsidedness of a galaxy is caused by merging, and such merging process is also causing the warping, we would expect more pronounced warps in lopsided galaxies, and small or no warps in axisymmetric galaxies.

The first indication that lopsidedness may be the result of accretion or interactions with nearby companions comes from the fact that the lopsidedness we measure seems to depend quite strongly on the environment. In Fig. 6 we have plotted histograms for the galaxies according to their density lopsidedness index for each type of environment: poor, intermediate and rich (see Sect. 4.8). Clearly, galaxies with no nearby companions are quite symmetric in mass, galaxies with companions not closer than 50″ are somewhat more lopsided, and
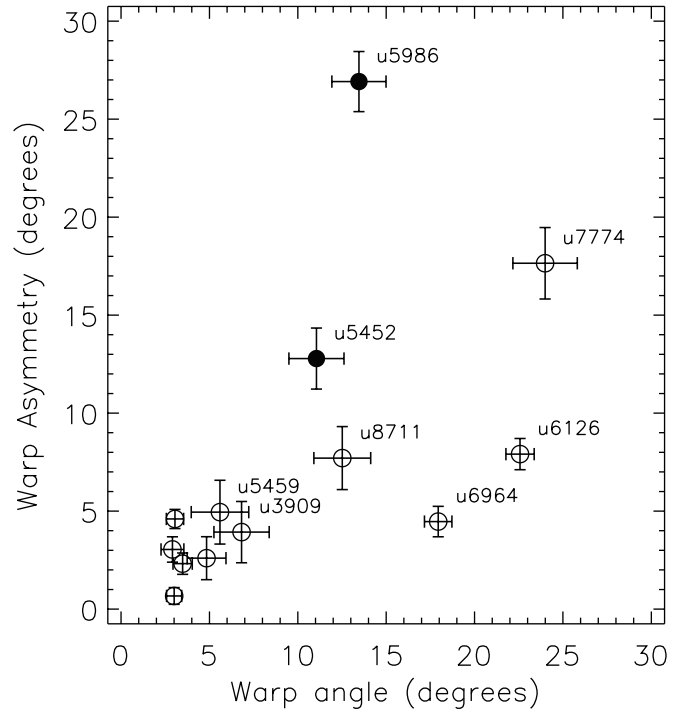

Fig. 5. Warp asymmetry vs. mean warp angle. Filled circles represent galaxies with obvious tidal features with nearby companions, thus indicating strong interaction. The most strongly warped galaxies are identified by their UGC number.

finally, all galaxies with a lopsidedness greater than 5% have a companion closer than 50″. The dependence of lopsidedness on environment found here is remarkable if one takes into account the uncertainty of the classification of the environment. The kinematical lopsidedness seems also to depend somewhat on the environment, as isolated galaxies have lower kinematical lopsidedness than the rest of the galaxies. The way both lopsidedness indices are measured actually makes them lower limits due to the fact that the galaxy is edge-on: to measure our lopsidedness indices we are comparing the approaching and receding sides of the galaxy (integrated along the line of sight), thus if the galaxy is asymmetric in the direction along the line of sight we would not be able to detect it. We did not find a clear correlation between kinematic and density lopsidedness in our galaxies.

5.3. The radial HI profile and warping

5.4. Warps and environment

The lopsidedness seems to be correlated with the environment, in the sense that in rich environments galaxies are more lopsided. It has been claimed (Reshetnikov & Combes 1998) that optical warps also depend on the environment, in the sense that galaxies in rich environments are more commonly warped than isolated galaxies. These authors concluded that this could indicate that tidal interactions are the cause of warps, or at least that they reinforce them. In a study of the influence of minor mergers on the warping of optical disks Schwarzkopf & Dettmar (2001) found warps in all their merging systems, but in only
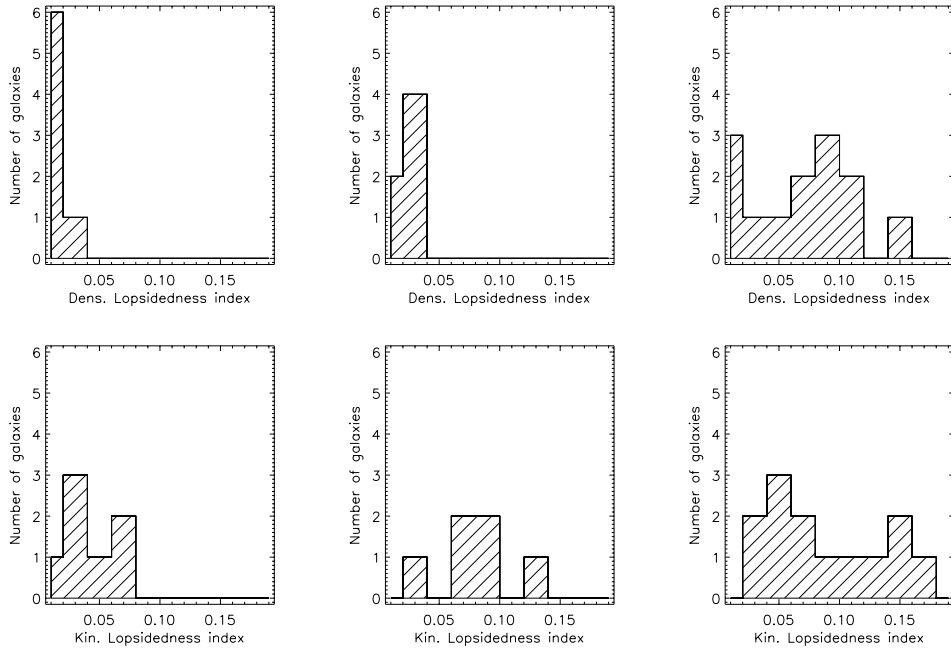
Fig. 6. Histograms showing the distribution of galaxies according to the density (upper panels) and kinematical (lower panels) lopsidedness index for different environments. Galaxies in poor environments are plotted in the left panels, galaxies in intermediate environments in the middle panels, and galaxies in rich environments in the right panels. For a detailed description of the environment classification, see Sect. 4.8.

Table 6. Comparison of warps in the optical (Sánchez-Saavedra et al. 1990) and HI (this work). The first two columns show the NGC and UGC names, and the third and fourth columns show the sense of the detected warp, which can be either N (anti-clockwise), S (clockwise) or U (bowl shaped). NGC 5229 doesn't have a clear detected warp in HI.

Galaxy		Optical	HI
(NGC)	(UGC)		
3432	5986	–	U
3510	6126	N	N
3600	6283	N	S
4010	6964	N	S
4144	7151	–	–
5023	8286	–	N
5229	8550	S	S?
5297	8709	–	–
5301	8711	N	N

half of their control sample. The amplitude of the warps in the merging systems was larger as well. They concluded that tidal interaction does generate warps but that this mechanism does not account for all the observed ones.

We checked our sample to see if these relations hold for the larger HI warps as well. Table 5 shows that, if anything, the trend in frequency for the occurrence of HI warps in our sample seems to go in the opposite sense: galaxies in poor environments are more frequently warped than galaxies in dense environments. However, all galaxies with an extended HI disk with respect to the optical disk are warped, therefore the frequency of warps depends on the extension of the HI disks. Thus, in our sample there are more galaxies with no extended HI in rich environments than in poor environments. The warp parameters

(amplitude and asymmetry) are illustrated as a function of environment in Fig. 8.

There seems to be a tendency for galaxies in poor environments to be more prone to warping, but to have smaller warp angles than in rich environments. Warps also seem to be more symmetric in poor than in rich environments. The explanation for the asymmetry and higher amplitude of the warps in rich environments could lie in the tidal interaction with neighboring galaxies (e.g. UGC 5452, UGC 8396). The indication that galaxies in poor environments are more frequently warped may mean that tidal interactions are not the only mechanism that produces warps.

5.5. HI vs. optical warps

As mentioned above, warps may show a different behavior with respect to environment when observed in the optical or in HI. Unfortunately, not much work has been done about the relationship between HI and optical warps in the same galaxies, and none with high quality HI and optical data.

Sánchez-Saavedra et al. (1990) studied optical warps using POSS plates. They looked at all NGC galaxies in the northern hemisphere that had $\log R_{25}$ larger than 0.57, and determined whether the warp was clockwise or anti-clockwise (S or N warps). Nine of their galaxies are in our sample, so we decided to compare with our results and find out whether the sense of the warp is the same or not. Table 6 shows the results. Four of the galaxies in common do not appear to be warped in the Sánchez-Saavedra et al. (1990) study. Two of the warped galaxies have the same sense as found in this work, two the opposite, and the last one has a dubious warp in HI. In the case of UGC 6964 the difference may be due to dust and/or spiral
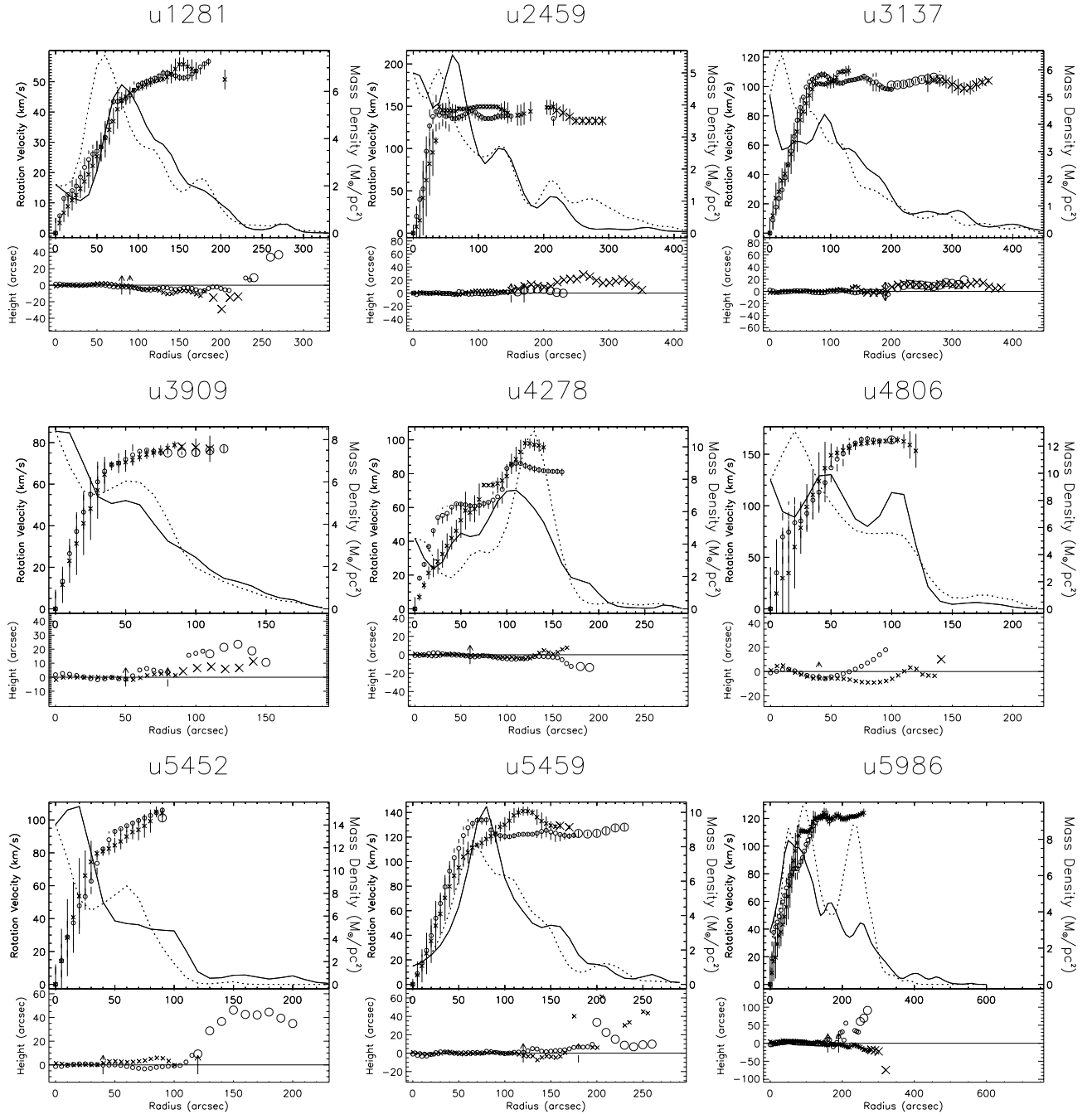
Fig. 7. Density – RC – warp plots. For each galaxy, the rotation curve along the major axis, the radial HI density profile and the curve of warp are plotted. We have measured these quantities independently for both sides of the galaxies, and here we present them together in the same plot. The top panel shows the rotation velocities and radial density profiles for both sides of the galaxy. The left axis shows the units for the rotation velocities, while the right axis applies to the density profiles. The bottom panel shows the warp curves for both sides. Because most of the warps have an S-shape, the warp curve derived for the left side has been inverted, to highlight symmetries or asymmetries between the two sides of the galaxy. With this process, both warp curves of a galaxy with a perfect S-shape symmetry (thus, antisymmetry) would fall on top of each other. One side is plotted with crosses (rotation curve and warp curve) and dotted line (density), and the other side is plotted with circles (rotation curve and warp curve) and solid line (density). The rotation curve and warp curves in the figure are shown at 2 different resolutions. We derived these curves using the full resolution data (small symbols), and then complemented it in the outer parts with the curves obtained at 30″ resolution (bigger symbols). Errorbars have not been plotted in the warp curves for sake of clarity, they are shown in Fig. 13.

arms. The optical image shows patchy emission and it indeed looks bent with an "N" shape, while the HI bends in the opposite direction in quite a spectacular way. In the other case, UGC 6283, the difference is probably due to the shape of the

warp curve itself. The disk bends first slightly in one direction, turns back and then bends in the opposite direction. The warp seen in the optical is probably tracing that first small "kink" of the warp shape. So in this case the warp is correctly detected,

u6126   u6283   u6964

u7089   u7090   u7125
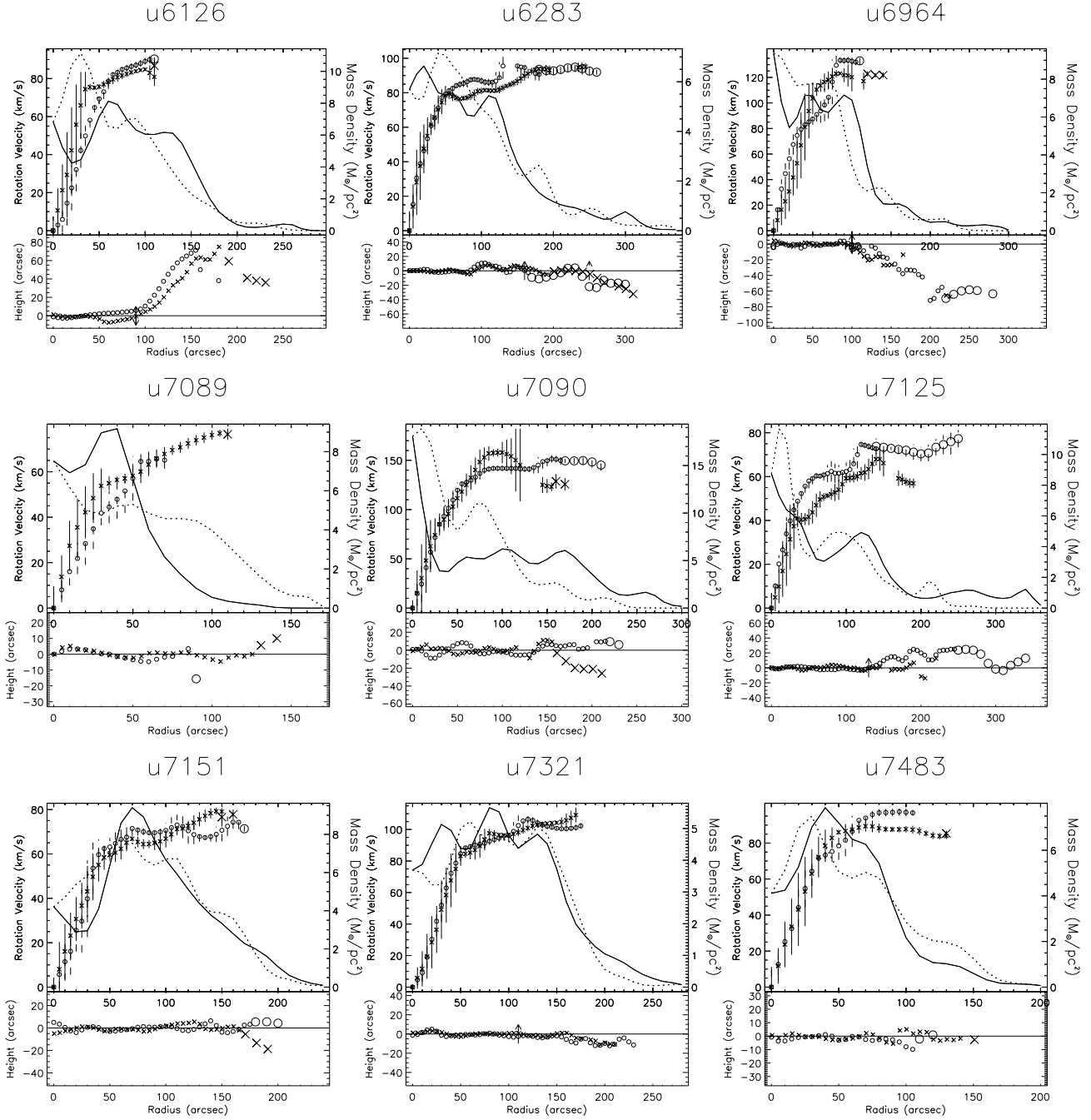
u7151   u7321   u7483

Fig. 7. continued.

but the general sense of the warp is not, because the optical disk ends before the HI warp changes direction. This galaxy is not completely edge-on and it is possible that this "kink" could be due to the presence of spiral arms.

Our conclusion from this comparison is that the stellar warps studied thus far are not directly comparable to the HI warps. The latter occur at larger galactocentric radius, and generally have a considerably higher amplitude. At this point it is unclear whether (faint) stellar disks extend to these radii or not.

In our search for a common property among warped galaxies (with respect to the non warped ones), we have com-

pared the radial HI profiles of both types of galaxies. We have excluded galaxies that are interacting with nearby neighbors, because a tidal interaction probably affects the radial profile of a galaxy. We also removed galaxies with very small warps. Thus we have constructed two groups of galaxies: the bona fide warped galaxies, UGC 1281, 2459, 3137, 3909, 5459, 6964, 7125, 7321, 7774, 8286 and 8711; and the *non*-warped galaxies UGC 7089, 7090, 7151, 7483, 9242.

We have scaled the radial profiles using $R_{\rm HI}$ as unit radius and the radial densities with $M_{\rm HI}/D^2$, where D is the distance to the galaxy. We have tried other scaling factors (such as the
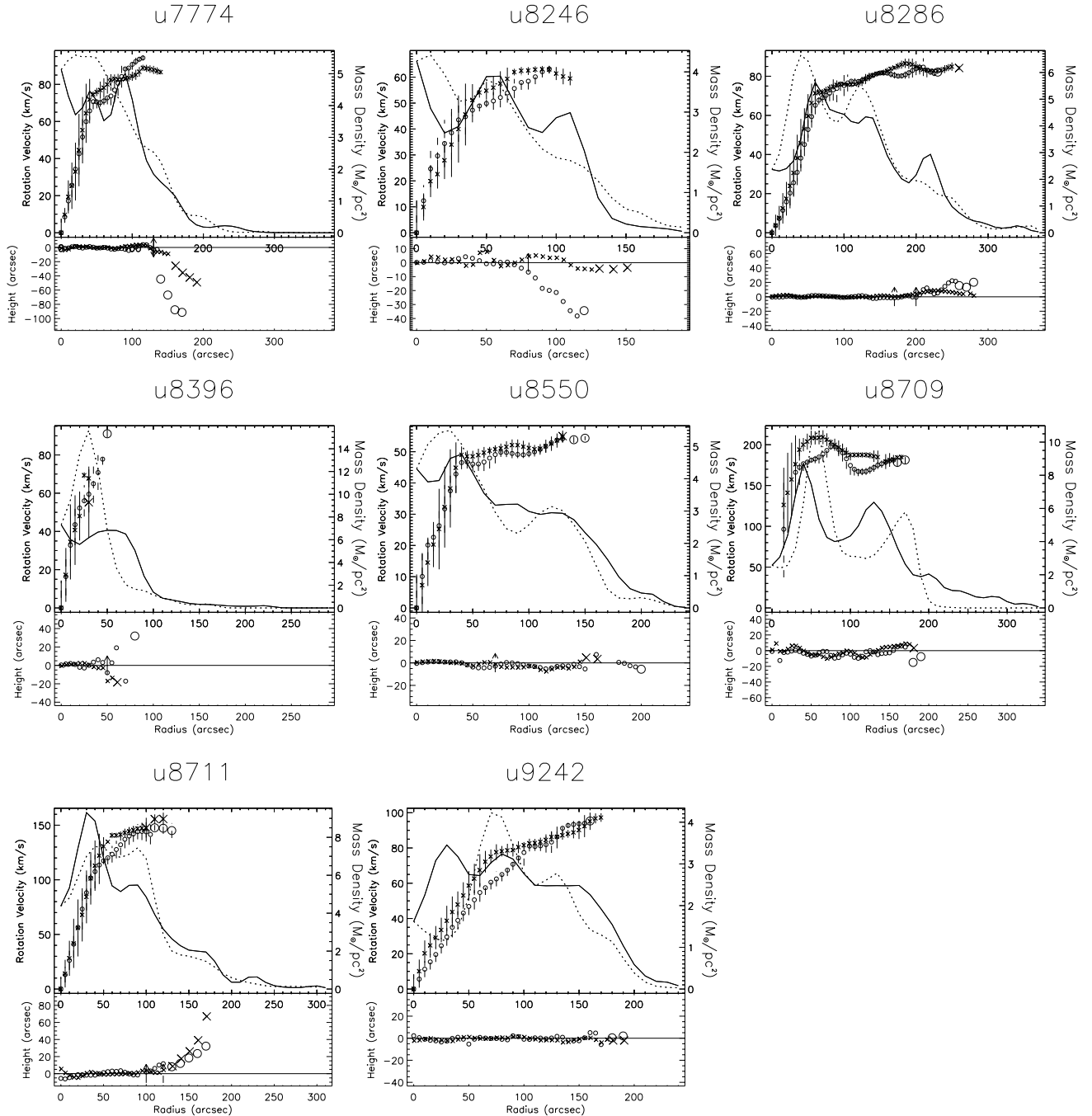
Fig. 7. continued.

radius where the density drops to 0.5 the peak density; and the area below the profile) with no effect on the conclusions presented here.

Figure 9 shows the individual profiles as well as the mean profile for each group of galaxies. A histogram showing the radius at which warps begin is also plotted. These plots show that warped galaxies are more extended in HI than non warped galaxies: at around 1.1 R_{HI} the HI density of a galaxy with no warp falls much faster than that of a warped galaxy, which still has some more gas extending up to 1.5 and even 2 R_{HI}. This extra gas we see in the warped galaxies is the same feature as the "shoulder" mentioned in Sancisi (1983).

Thus, the typical radial HI profile of a warped galaxy has the following shape: in the inner parts it is roughly constant or slowly decreases, around 0.5 R_{HI} it drops faster, and further out it extends at low levels ending at 1.5–2 R_{HI}. It is in the second part of the profile (the steepest part, around the optical edge) where a warp develops in most of the galaxies.

We have also measured the extent of the HI with respect to the optical in both non warped and warped galaxies. Figure 10 shows the histograms for both groups, and indicates that warped galaxies have HI layers more extended with respect to the optical than galaxies with no warps. There is no galaxy in our sample with an extended HI disk with respect to the optical disk and no warp.
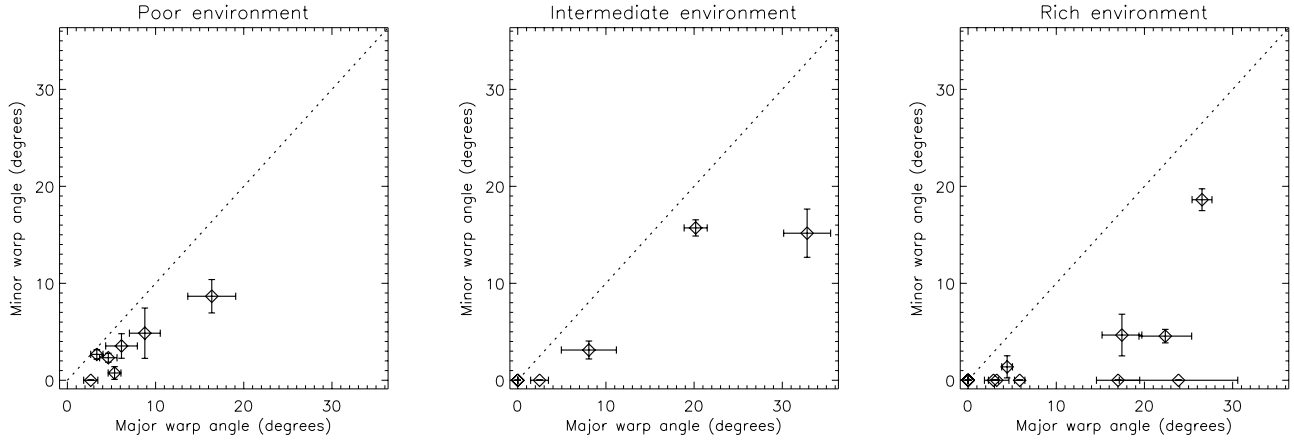
Fig. 8. Warp angles for each environment class (see definition in Sect. 4.8). The left panel shows the warps of galaxies in poor environments, the middle panel the galaxies in intermediate environments, and the right panel those in rich environments. For each galaxy, the larger of both side's warp angles has been plotted on the *x* axis, versus the smaller one on the *y* axis (so the upper left part of the plots is empty). The galaxies with a detected warp on only one side lie in the $y = 0$ line, and the non warped galaxies are in the origin. The dotted line indicates equal warp angles on both sides of the galaxy.
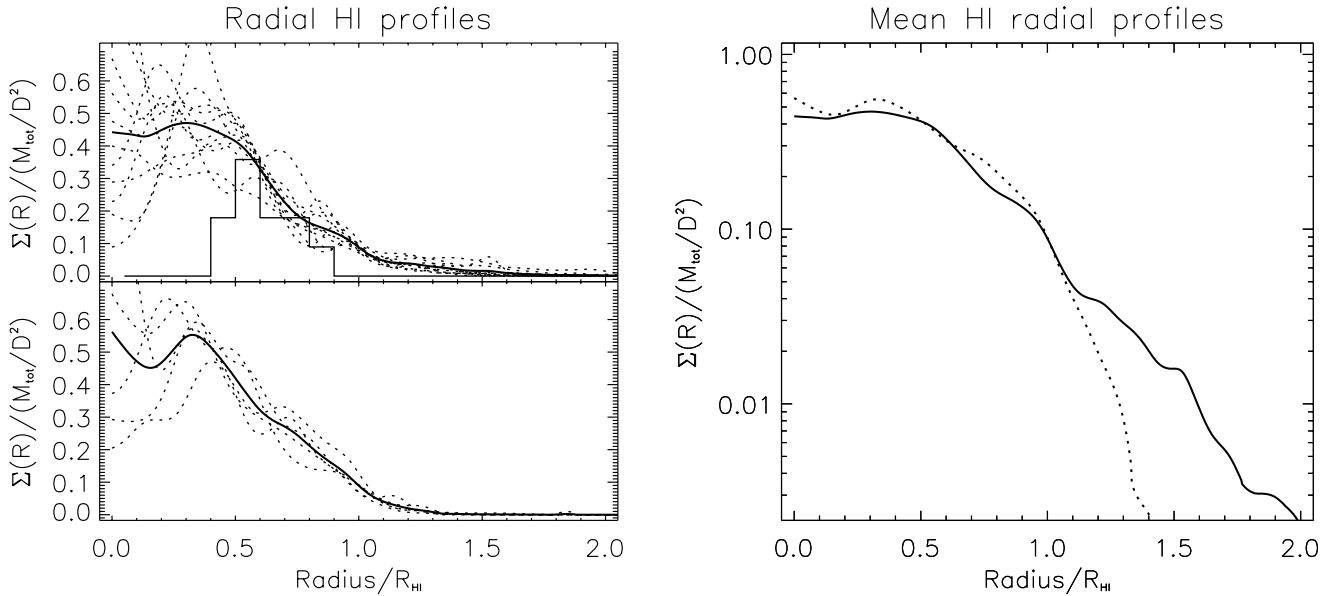

Fig. 9. Radial HI density profiles. The plot on the left shows the HI profiles for bona fide warped (upper panel) and *non*-warped (lower panel) galaxies (see Sect. 5.3 for definition of both groups). The profiles of individual warped and non warped galaxies are plotted in dotted line, and the thick line is the average profile for each group. In the upper panel a histogram of the radius where the warp begins is overplotted. We have treated both sides of the galaxy independently, to take into account that two of our bona fine warped galaxies have only one-sided warps. The plot on the right shows the mean profiles for both bona fide warped (solid line) and *non* warped galaxies (dotted line).

5.6. Warp amplitudes

We have plotted the warp amplitude (warp angle) vs. the width of the global HI profile at 20% level and vs. the extent of the HI with respect to the optical in Fig. 11. The objects with obvious interaction with nearby companions are shown with large filled symbols. For this class of objects there seems to be a relation between the width of the profile and the warp amplitude in the sense that galaxies with broader profiles have smaller warps.

For the rest of the galaxies we have not found any relation with either the visible mass of the galaxy or the width of the global HI profile. If warps are caused by some force realigning the disk of the galaxy (as opposed to inflow of HI gas at a

different angle than that of the inner disk), this means that the force should scale (on average) with the mass of the system. The amplitude of warps does not seem to be related to either the density lopsidedness or the kinematical lopsidedness. The same is true for the asymmetry of warps.

Figure 11 also shows the amplitude of the warps vs. the HI extent with respect to the optical. We can see that non warped galaxies are at low R_{HI}/R_{opt}, and that large warps only occur in galaxies with large R_{HI}/R_{opt}.

5.7. Mean surface density

It has been shown that there is a tight relation between HI mass and HI radius (Broeils & Rhee 1997; Verheijen 1997),
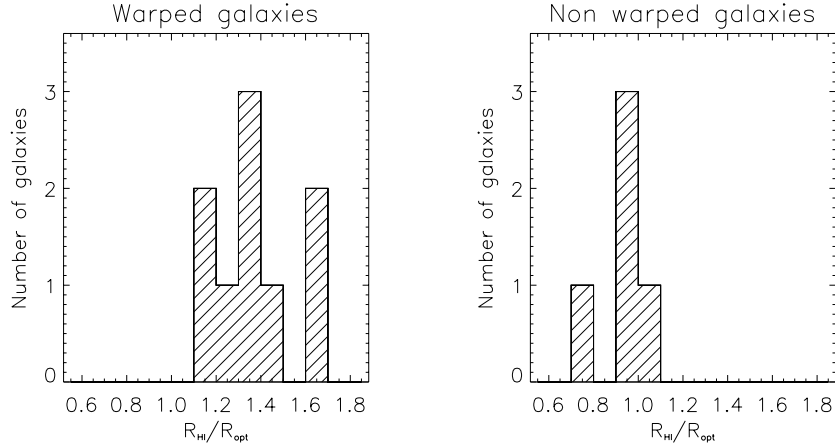
Fig. 10. Histograms of the ratio $R_{\rm HI}$ to $R_{\rm opt}$ for bona fide warped (left panel) and *non*-warped (right panel) galaxies (see Sect. 5.3 for definition of both groups). The histograms show that warped galaxies are more extended in HI than the non warped ones.
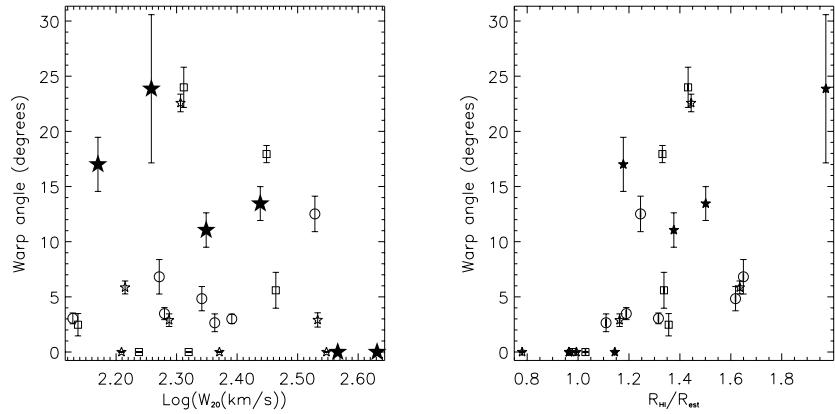

Fig. 11. Warp amplitude vs. the width of the global HI profile at 20% level (left) and vs. $R_{\rm HI}/R_{\rm opt}$ (right). The symbols indicate different environmental conditions: isolated (open circles), intermediate (squares), rich environment (empty stars) and interacting (filled large stars). For a detailed description of the environment classification, see Sect. 4.8.
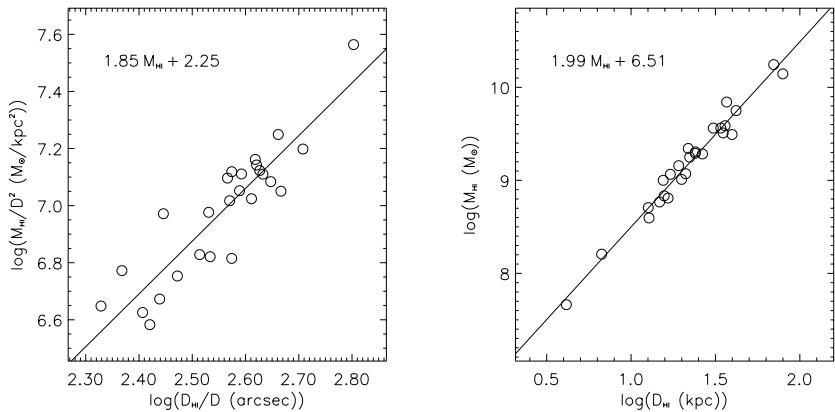

Fig. 12. HI mass vs. HI radius for all the galaxies in the sample. The left panel shows the relation among measured quantities ($M_{\rm HI}/D^2$, $D_{\rm HI}/D$, where D is the distance to the galaxies), while the right panel shows the relation after the distance has been used to derive linear diameters and masses of the galaxies.

with a slope close to 2 in a log-log scale. Figure 12 shows both $M_{\rm HI}/D^2$ vs. $D_{\rm HI}/D$ relation (measured quantities) and $M_{\rm HI}$ vs. $D_{\rm HI}$ (after multiplication by the distance to each galaxy). The slope of the relation changes from 1.85 to 1.99 in these plots, which illustrates how uncertainty in the distances to the

galaxies can artificially "enhance" relations and alter the slopes. But even a slope of 1.85 implies that the average HI surface density ($\langle\sigma_{\rm HI}\rangle$) is more or less constant from galaxy to galaxy. The average value is $4.0 \pm 1.0\ M_\odot\ {\rm pc}^{-2}$, consistent with the measurements by Broeils & Rhee (1997).

Table 7. Companions to the galaxies in the sample within 100 arcmin. We have only considered galaxies that have a heliocentric velocity that differs less than 150 km s^{-1} from that of the host galaxy, or have a clear pattern of interaction with it. We present the names of the host galaxy, the names of the companions, positions, distances of the companions to the host galaxy, heliocentric velocity from NED, and measured heliocentric velocities.

Galaxy	Companion	RA	Dec	dist	V_{NED}	V_{HI}
1281		01 46 38.1	32 20 15		157	157
2459		02 57 08.4	48 50 43		2464	2469
	HFLLZOA G144.00-08.53	02 58 57.7	48 43 03	19.6		2456
3137		04 39 22.4	76 19 37		992	993
3909		07 30 54.0	73 49 28		945	943
4278		08 10 27.4	45 53 43		563	555
	NGC 2537A	08 10 09.0	46 08 46	15.4	443	
	NGC 2537	08 09 42.6	46 08 32	16.7	447	445
4806		09 06 30.2	33 19 38		1947	1948
	KUG 0906+333A	09 06 16.0	33 19 31	3.0		≃1850
	—––-	09 06 43.2	33 20 52	3.0		≃1970
	—––-	09 06 58.3	33 09 14	11.9		≃2020
	IC 2445	09 10 10.9	32 00 53	91.4	1968	
	CG 0010	09 09 50.3	32 53 15	96.1	1860	
	UGC 04777	09 03 34.8	32 49 14	96.7	2052	
5452		10 04 17.1	33 16 20		1342	1340
	UGC 5446	10 03 36.3	33 11 27	9.8	1383	1362
	UGC 5482	10 07 22.9	33 31 23	59.5	1466	
	KUG 1006+322	10 06 04.2	33 15 22	65.0	1390	
	UGC 5393	09 58 46.3	33 22 41	69.4	1448	
5459		10 04 54.7	53 19 39		1112	1109
	UGC 5460	10 04 55.0	52 05 20	74.3	1093	
	UGC 5479	10 06 51.9	54 44 53	87.0	1105	
5986		10 49 42.9	36 53 09		616	615
	UGC 5983	10 49 27.4	36 51 36	3.5	(1)	
	SBS 1054+365	10 54 59.8	36 31 30	67.1	603	
	VV 747	10 55 00.2	36 31 43	67.1	634	
	CGCG 184-040 NED02	10 55 00.0	36 31 00	67.3	665	
6126		11 01 00.6	29 09 17		705	704
	[M98k] 110110.0+285730	11 01 10.0	28 57 30	12.1		≃660
	UGCA 225	11 02 15.6	29 24 34	22.4	646	≃640
	UGC 6102	10 59 05.2	28 57 30	27.8	702	≃700
	NGC 3486	10 57 40.4	29 14 37	44.0	681	
	BTS 026	10 57 57.0	29 58 18	63.2	675	
6283		11 13 06.5	41 51 50		719	713
6964		11 56 02.9	47 32 20		907	902
	NGC 3949	11 51 05.2	48 08 13	61.5	807	
	NGC 3985	11 54 06.8	48 36 44	67.3	950	
	UGCA 259	11 56 18.8	46 00 46	91.6	1154	
	MRK 1460	11 48 12.8	48 31 46	98.5	768	
7089		12 03 25.6	43 25 25		776	774
	UGC 7094	12 03 38.5	43 14 05	11.6	780	786
	NGC 4111	12 04 31.0	43 20 37	12.8	807	
	MAPS-NGP O_217_0067378	12 03 26.8	43 10 52	14.5	756	
	NGC 4117	12 05 14.1	43 24 17	19.7	943	
	NGC 4118	12 05 20.8	43 23 22	21.0	661	
	NGC 4138	12 06 58.6	43 57 46	50.3	888	
	NGC 4143	12 07 04.8	42 48 43	54.3	985	
	IC 0750	11 56 17.6	43 00 92	82.0	701	
	IC 0749	11 55 59.5	43 00 44	84.9	784	
	NGC 4183	12 10 46.6	43 58 33	86.3	930	
	NGC 4051	12 00 36.4	44 48 35	88.5	725	
	UGC 7129	12 06 23.4	42 01 10	90.3	926	
	NGC 4013	11 55 56.6	44 13 32	94.2	834	

(1) No velocity available, but the optical image shows interaction with UGC 5986.

Table 7. continued.

| Galaxy	Companion	RA	Dec	dist	V_{NED}	V_{HI}
7090		12 03 28.5	47 45 20		566	581
	PC 1200+4755	12 00 26.7	47 55 57	32.3	600	
	NGC 4144	12 07 27.5	46 44 09	73.4	265	
7125		12 06 10.2	37 04 51		1071	1072
	UGC 7207	12 09 47.8	37 17 30	45.2	1051	
	UGC 7257	12 12 32.1	36 14 13	91.8	942	
7151		12 07 27.5	46 44 09		265	263
	NGC 4096	12 03 28.5	47 45 20	73.4	566	
	NGC 4242	12 15 01.2	45 53 47	93.1	517	
	MRK 1471	12 15 21.9	47 41 10	98.7	484	
7321		12 15 02.0	22 49 05		408	407
7483		12 21 41.8	31 47 56		1253	1247
	UGC 7428	12 19 32.6	32 22 21	44.0	1137	
	KUG 1218+310	12 18 05.6	31 04 36	63.3	1010	
	NGC 4314	12 20 01.8	30 10 21	99.9	963	
7774		12 33 57.4	40 16 49	526	527	
	UGC 07678	12 29 34.4	40 06 32	51.3	685	
	UGC 7751	12 32 46.6	41 20 10	64.8	605	
	UGC 7719	12 31 34.6	39 17 42	65.2	681	
	UGCA 290	12 34 56.5	39 01 08	76.5	445	
	NGC 4618	12 39 09.0	41 25 29	90.5	544	
	NGC 4625	12 39 29.0	41 32 50	98.5	609	
8246		13 07 44.3	34 26 47		813	807
	NGP9 F269-1340356	13 08 09.0	34 30 09	6.1		≃850
	UGC 8323	13 12 29.3	35 08 42	72.0	856	
	UGC 8261	13 08 41.9	35 46 00	80.1	852	
	IC 4213	13 09 52.1	35 56 11	93.1	815	
	UGC 8181	13 03 02.9	33 10 02	96.5	886	
8286		13 09 58.1	44 18 14		407	406
8396		13 19 09.3	38 47 57		946	947
	NGC 5112	13 19 41.4	38 59 44	13.3	965	971
	UGC 8315	13 11 53.6	39 24 41	92.2	1164	
8550		13 31 58.4	48 10 16		364	359
	MESSIER 051b	13 27 52.4	47 31 32	56.6	465	
	MESSIER 051a	13 27 46.0	47 27 22	60.3	463	
	SBS 1331+493	13 31 19.5	49 21 28	71.5	599	
8709		13 44 18.4	44 07 18		2407	2402
	NGC 5296	13 44 13.5	44 06 02	1.5	2224	
	UGC 08733	13 46 33.8	43 39 37	36.9	2338	
	UGC 08798	13 50 44.5	44 04 25	69.4	2275	
	NGC 5336	13 50 05.4	43 29 21	73.2	2338	
8711		13 44 21.4	46 21 25		1503	1506
9242		14 23 19.7	39 45 50		1440	1438
	NGC 5582	14 18 41.3	39 55 18	54.3	1435	
	MRK 0676	14 17 23.7	40 05 11	70.9	1734	
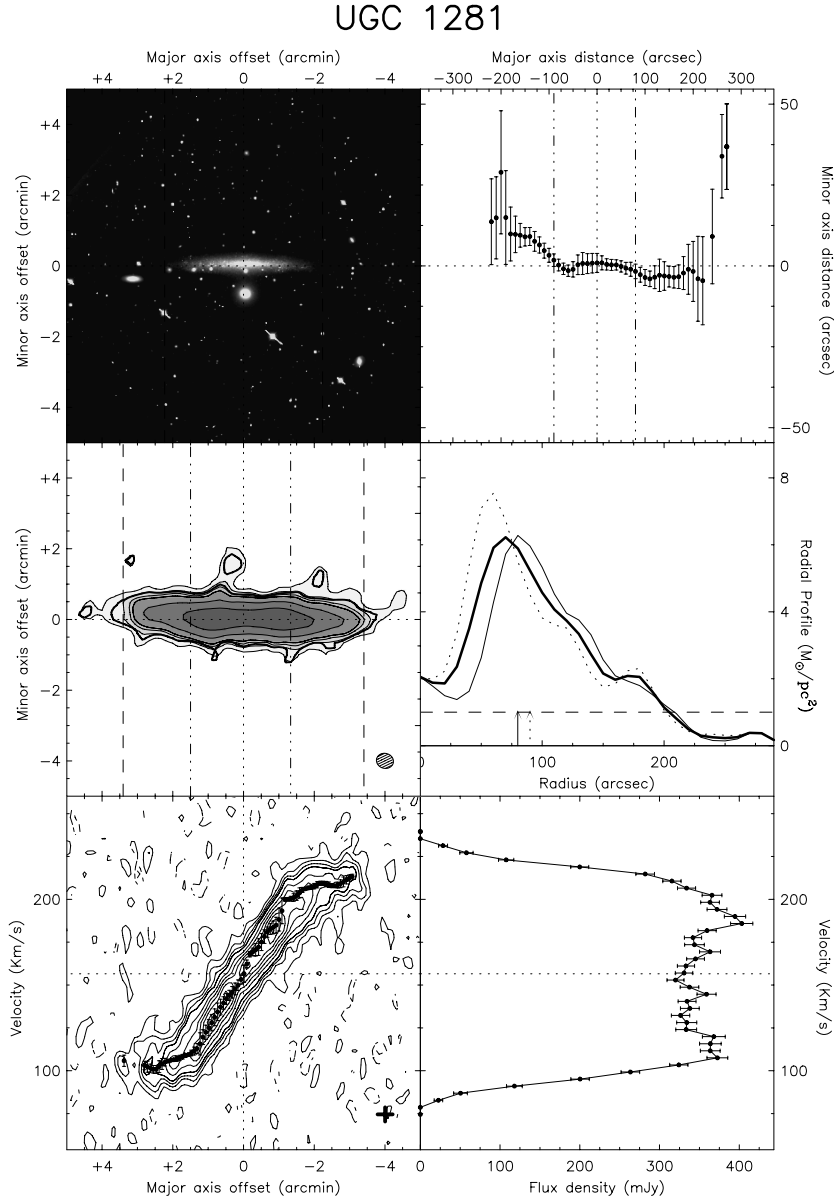
UGC 1281

Fig. 13. The HI and optical data for UGC 1281; the corresponding figures for the other galaxies in the sample are only available in the online version. For each galaxy we have created a six panel figure, we present an overview of the HI and optical data for all the galaxies in the sample. For each galaxy we have created a six panel figure, in which we have displayed the relevant information. We have used the 30″ resolution data for the HI except for the XV diagram where we used the full resolution data. These panels are available in electronic form in the WHISP pages (http://www.astro.rug.nl/~whisp). For each galaxy we have tabulated the rotation curve, the HI radial surface density profile and the warp curve. There is extra material as well that supplies extra velocity information. *Top left*: *R*-band optical image, rotated so that the major axis of the galaxy is on the horizontal axis. Vertical dashed lines have been plotted at R_{25}. *Top right*: Warp curve derived from the total intensity HI map using the method described in Sect. 4.6. Note that the scale is not the same in the horizontal and vertical axes, and that this ratio differs from galaxy to galaxy. This allows the reader to follow the warp curve more precisely. A plot with the same scale on both axes is shown in Fig. 7. The vertical dot-dashed lines mark the warp radius. *Middle left*: total HI map. The thick contour is the locus of the points that have three sigma rms noise as defined in Sect. 4.1. Note that this does not mean that the line profiles have emission at three sigma level, as low-level emission may add-up to more than three sigma. The other contours levels are at 1, 2, 3, 4, 8, 16,... times the lowest contour, whose level is indicated in the caption of each galaxy. The beam size is indicated by the symbol at the lower right, R_{HI} (radius at 1 $M_\odot/pc^2$) by vertical dashed lines and the warp radii by vertical dash-dotted lines. *Middle right*: radial HI surface density profile. The right (left) side is plotted in solid (dotted) lines and the mean profile with a thick line. Section 4.4 explains how the observed integrated emission is deconvolved to derive the radial profile. The solid (dotted) arrow indicates the warp radius for the right (left) side of the galaxy. In the cases where the warp radius is the same for both sides a double-head arrow is plotted. *Bottom left*: position-velocity (heliocentric) diagram along the major axis of the galaxy. Full resolution data are plotted here. For a more extended rotation curve determined combining high resolution and 30 arcsec resolution data, see Fig. 7. Contours have been drawn at -3σ, -1.5σ, 1.5σ, 3σ, 4.5σ, 6σ, 9σ, 12σ,... (the value of 3σ is indicated in the caption of each galaxy). Negative contours are dashed. The derived rotation curve (see Sect. 4.5) is shown as black dots with error bars. Note that these maps give the HI distribution only along the major axis and, therefore, do not contain the warped HI. *Bottom right*: global profile, with the systemic velocity indicated by the dotted horizontal line.

There seems to be a trend of the mean surface density with respect to the asymmetry of warps, in the sense that galaxies with larger mean surface densities seem to possess more symmetric warps.

6. Conclusions

We have studied the warps in the outer HI layers of a sample of 26 edge-on galaxies with particular attention to warp amplitudes, asymmetry, occurrence rates and their relationship with the environment. We have also studied the density and kinematic lopsidedness of the HI disks.

There are indications that environment may play a role in warping. It is claimed that in rich environments optical warps seem to be larger and more frequent (Reshetnikov & Combes 1998), and HI warps are larger and more asymmetric. However, the ubiquity of warps, even in low density regions and the symmetry of some warps suggest that their origin is not simply the result of interactions with the environment. The fact that all galaxies with an HI layer more extended than the optical show warps of very different amplitudes could indicate that warping is similar in a way to spiral structure. Most perturbations of a disk galaxy, arising e.g. from companions or secondary infall, will provoke a warped response.

The universality of this response makes it hard to pinpoint the perturbation that preceded it. While the trend with environment suggests that tidal effects play an important role, it seems likely that there are other, perhaps more intrinsic, effects at work that cause even quite isolated galaxies to warp. In this sense, the situation may be similar to that for spiral structure, another universal response whose origin is not clear in all details.

Late infall of HI gas might be responsible for the warps we detect. This would explain the "extra" HI gas that warped galaxies have outside R_{HI} while the inner profiles of warped and non warped galaxies are similar. This late infall might cause star formation at the outskirts of the optical disk that could be detected in Hα imaging or by looking at its color.

To summarize, we list the main conclusions:

- We detect warps in 20 out of our 26 sample galaxies confirming that warping of the HI disks is a very common phenomenon in disk galaxies. In fact all galaxies that have an HI disk more extended than the optical are warped.
- The amplitude of warps varies considerably from galaxy to galaxy. Also for a given galaxy there can be a large asymmetry in amplitude and shape between the two sides. A large number of warps in our sample are asymmetric. Most of the galaxies with both sides warped are antisymmetric (S shape warps). We only have two cases of U-type warps, and both galaxies are strongly interacting with nearby companions and are very disturbed.
- The warping of the disks usually starts near the edge of the optical disk where the HI density drops down.
- The connection between HI and optical warps is not clear. HI warps are found in general at larger radii than the optical ones, and as a consequence they probe a different region of the potential of the galaxy. A joint optical+HI study of

warps could give important insights on the formation mechanism(s) of warps.
- There seems to be a dependence of warps on environment in the sense that galaxies in rich environments tend to have larger and more asymmetric warps than galaxies in poor environments.
- The presence of density lopsidedness (and in a weaker way that of kinematical lopsidedness) seems to be related to the presence of nearby companions.

Appendix A: Determination of the warp radius on an edge-on galaxy

In this appendix we explain how we have determined the warp radius for our galaxies using Gaussian fits perpendicular to the major axis of the galaxy. We take both the centroids of the Gaussian fits (we refer to them as datapoints) and their uncertainties (σ_i). The basic idea is to determine the radius at which the galactic disk begins to bend away from the plane defined by the inner disk in a systematic way.

We take the innermost $R_{25}/2$ part of the disk as the inner disk, which we assume is flat. We fit a straight line to it and determine the vertical offset and the dispersion (σ_{inner}). The offset will correct (to first order) possible errors in the determination of the center of the galaxy, and we can use the dispersion as an estimate of how noisy our disk is (influence of not completely edge-on spiral arms and other irregularities). We then define the warp radius as the location where a significantly large portion of the disk (at least $R_{25}/4$) departs coherently more than $\sigma_{inner} + \sigma_i$ from the plane defined by the inner disk. σ_i are the uncertainties of the individual datapoints in the warped portion of the disk.

If the uncertainties in the datapoints are large we could miss some warps with this procedure. Even with large errors, a coherent smooth warp could be detected if we smooth the warp curve and apply the procedure again. Thus we smooth the warp curve to different resolutions and determine a preliminary warp radius at each resolution. The final warp radius is the minimum value of all the preliminary values. The outcome of this method is shown in the Atlas in Fig. 13, where warp curves and warp radii are shown on the same panel.

References

Avner, E. S., & King, I. R. 1967, AJ, 72, 650
Battaner, E., Florido, E., & Sanchez-Saavedra, M. L. 1990, A&A, 236, 1
Bertin, G., & Mark, J. W.-K. 1980, A&A, 88, 289

Bosma, A. 1991, in Warped Disks and Inclined Rings around Galaxies, ed. S. Casertano, P. D. Sackett, & F. Briggs (Cambridge: Cambridge Univ. Press), 181

Bottinelli, L., Gouguenheim, L., Fouqué, P., & Paturel, G. 1990, A&AS, 82, 391

Burke, B. F. 1957, AJ, 62, 90

Briggs, F. 1990, ApJ, 352, 15

Broeils, A. H., & Rhee, M. H. 1997, A&A, 324, 877

Burton, W. B. 1988, Galactic and Extragalactic Radio Astronomy, ed. G. L. Verschuur, & K. I. Kellerman (Springer-Verlag), 295–358

Debattista, V. P., & Sellwood, J. A. 1999, ApJ, 513, L107

Dickey, J. M., Hanson, M. M., & Helou, G. 1990, ApJ, 352, 522

Dubinski, J., & Kuijken, K. 1995, ApJ, 442, 492

Goad, J. W., & Roberts, M. S. 1981, ApJ, 250, 79

Haynes, M. P., Hogg, D. E., Maddalena, R. J., Roberts, M. S., & van Zee, L. 1998, AJ, 115, 62

Hunter, C., & Toomre, A. 1969, ApJ, 155, 747

Ing-Guey, J., & Binney, J. 1999, MNRAS, 303, L7

Kamphuis, J. 1993, Ph.D. Thesis, University of Groningen

Kerr, F. J. 1957, AJ, 62, 93

Kraan-Korteweg, R. C. 1986, A&AS, 66, 255

Lucy, L. B. 1974, AJ, 79, 745

Nelson, R. W., & Tremaine, S. 1995, MNRAS, 275, 897

Petrou, M. 1980, MNRAS, 191, 767

Porcel, C., Battaner, E., & Jiménez-Vicente, J. 1997, A&A, 322, 103

Reshetnikov, V., & Combes, F. 1998, A&A, 337, 9

Richter, O. G., & Sancisi, R. 1994, A&A, 290, L9

Robin, A. C., Creze, M., & Mohan, V. 1992, ApJ, 400, L25

Sánchez-Saavedra, M. L., Battaner, E., & Florido, E. 1990, MNRAS, 246, 458

Sancisi, R. 1976, A&A, 53, 159

Sancisi, R. 1983, Internal Kinematics & Dynamics of Galaxies, ed. E. Athanassoula (Dordrecht: Reidel), IAU Symp., 100, 55

Sancisi, R., & Allen, R. J. 1979, A&A, 74, 73

Tubbs, A. D., & Sanders, R. H. 1979, ApJ, 230, 736

Schwarzkopf, U., & Dettmar, R. J. 2001, A&A, 373, 402

Sparke, L. S., & Casertano, S. 1988, MNRAS, 234, 873

Swaters, R. A. 1999, Ph.D. Thesis, Groningen

Swaters, R. A., & Balcells, M. 2002, A&A, 390, 863

Swaters, R. A., Schoenmakers, R. H. M., Sancisi, R., & van Albada, T. S. 1999, MNRAS, 304, 330

Swaters, R. A., van Albada, T. S., van der Hulst, J. M., & Sancisi, R. 2001, in preparation

Taylor, C. L., Brinks, E., Pogge, R. W., & Skillman, E. D. 1994, AJ, 107, 3

Toomre, A. 1983, Internal Kinematics & Dynamics of Galaxies, ed. E. Athanassoula (Dordrecht: Reidel), IAU Symp., 100, 177

Uppsala General Catalogue of Galaxies, Uppsala Astr. Obs. Ann., vol. 6 (UGC)

Verheijen, M. A. 1997, Ph.D. Thesis, Univ. Groningen, The Netherlands

Verheijen, M. A. W., & Sancisi, R. 2001, A&A, 370, 765

Warmels, R. H. 1988, A&AS, 72, 427

West, M. J., & Blakeslee, J. P. 2000, ApJ, 543, L27